Evaluating the PurpleAir monitor as an aerosol light scattering instrument

James R. Ouimette[1], William C. Malm[2], Bret A. Schichtel[3], Patrick J. Sheridan[4], Elisabeth Andrews[4,5], John A. Ogren[6], W. Patrick Arnott[7]

[1]Sonoma Ecology Center, Eldridge, CA 95431, USA
[2]Cooperative Institute for Research in the Atmosphere, Colorado State University, Fort Collins, CO 80523, USA
[3]National Park Service Air Resources Division, Lakewood, CO 80225, USA
[4]NOAA Global Monitoring Laboratory, Boulder, CO 80305, USA
[5]Cooperative Institute for Research in Environmental Sciences, University of Colorado, Boulder, Colorado 80309, USA
[6]NOAA Global Monitoring Laboratory, Boulder, CO 80305, USA (Retired)
[7]Department of Physics, University of Nevada, Reno, NV 89557, USA
Correspondence to James R. Ouimette (JamesOuimette@sonomaecologycenter.org)

Abstract

The Plantower PMS5003 sensors (PA-PMS) used in the PurpleAir (PA) monitor PA-II-SD configuration are equivalent to cell-reciprocal nephelometers using a 657 nm perpendicularly polarized light source that integrates light scattering from 18 to 166 degrees. Yearlong field data at the National Oceanic and Atmospheric Administration's (NOAA) Mauna Loa Observatory (MLO) and Boulder Table Mountain (BOS) sites show that the 1 h average of the PA-PMS first size channel, labeled ">0.3 µm" ("CH1") is highly correlated with submicrometer aerosol scattering coefficients at the 550 nm and 700 nm wavelengths measured by the TSI 3563 integrating nephelometer, from 0.4 Mm^{-1} to 500 Mm^{-1}. This corresponds to an hourly average submicrometer aerosol mass concentration of approximately 0.2 to 200 µg m^{-3}. A physical-optical model of the PA-PMS is developed to estimate light intensity on the photodiode, accounting for angular truncation of the volume scattering function as a function of particle size. The model predicts that the PA-PMS response to particles >0.3 µm decreases relative to an ideal nephelometer by about 75% for particle diameters ≥1.0 µm. This is a result of using a laser that is polarized, the angular truncation of the scattered light, and particle losses (e.g., due to aspiration) before reaching the laser. It is shown that CH1 is linearly proportional to the model-predicted intensity of the light scattered by particles in the PA-PMS laser to its photodiode over 4 orders of magnitude. This is consistent with CH1 being a measure of the scattering coefficient and not the particle number concentration or particulate matter concentration. The model predictions are consistent with data from published laboratory studies which evaluated the PMS against a variety of aerosols. Predictions are then compared with yearlong fine aerosol size distribution and scattering coefficient field data at the BOS site. Field data at BOS confirm the model prediction that the ratio of CH1 to the scattering coefficient would be highest for aerosols with median scattering diameters <0.3 µm. The PA-PMS detects aerosols smaller than 0.3 µm diameter in proportion to their contribution to the scattering coefficient. The results of this study indicate that the PA-PMS is not an optical particle counter and that its six size fractions are not a meaningful representation of particle size distribution. The relationship between the PA-PMS 1 h average CH1 and b_{sp1}, the scattering coefficient in Mm^{-1} due to particles below 1 µm aerodynamic diameter, at wavelength 550 nanometers, is found to be $b_{sp1} = 0.015 \pm 2.07 \times 10^{-5} \times$

45   CH1, for relative humidity below 40%. The coefficient of determination r^2 is 0.97. This suggests
46   that the low-cost and widely used PA monitors can be used to measure and predict the submicron
47   aerosol light scattering coefficient in the mid-visible nearly as well as integrating nephelometers.
48   The effectiveness of the PA-PMS to serve as a $PM_{2.5}$ mass concentration monitor is due both to
49   the sensor behaving like an imperfect integrating nephelometer and to the mass scattering
50   efficiency of ambient $PM_{2.5}$ aerosols being roughly constant.

51   Keywords: PurpleAir, Plantower PMS5003, nephelometer, low-cost sensor, physical-optical
52   model, $PM_{2.5}$, scattering coefficient, visibility, atmospheric aerosol

53   1. Introduction

54   Currently there are tens of thousands of low-cost aerosol monitors used by atmospheric research
55   groups, air quality monitoring and regulatory organizations, and individual citizen scientists
56   around the world. The recent explosion in the number of these sensors (see, for example, Aerosol
57   Air Qual. Res. 20(2), 2020, Special Issue on Low-cost Sensors for Air Quality Monitoring and
58   papers therein) is a result of the increased research, regulatory, and citizen interest over the past
59   few years. For example, there are over 9,000 active PurpleAir (PA) aerosol monitors (PurpleAir
60   LLC, Draper, UT), with sampling locations on almost every continent. The large geographic
61   coverage of this array of low-cost sensors presents enormous potential for obtaining valuable
62   information on atmospheric aerosol properties and transport processes.

63   The majority of these low-cost aerosol sensors are used to monitor the mass concentration of
64   particles with aerodynamic diameters <2.5 μm ($PM_{2.5}$) (Kelly et al., 2017; Gupta et al., 2018;
65   Zheng et al., 2018; Sayahi et al., 2019; Barkjohn et al., 2020; Holder et al., 2020; Jayaratne et al.,
66   2020; Malings et al., 2020; Mehadi et al., 2020). However, these sensors do not actually measure
67   aerosol mass concentrations but light scattered by the aerosols and thus are dependent on the
68   aerosol particle size distribution, morphology, and composition. Recently, Hagan and Kroll
69   (2020) developed a framework and computer model to estimate the effects of relative humidity
70   (RH) and aerosol refractive index on $PM_{2.5}$ estimated by a number of low-cost sensors. Their
71   model assumed that the low-cost sensor lasers were not polarized and could be modeled with
72   Mie theory. The PMS5003 (PMS) was included in their classification scheme as an example of a
73   sensor that behaved more like a nephelometer than an optical particle counter.

74   Three recent laboratory studies showed that the PMS response decreases with particle size. He et
75   al. (2020) measured the PMS response to monodisperse ammonium sulfate aerosol particles
76   having diameters of 0.1, 0.3, 0.5, and 0.7 μm. The PMS was able to detect 0.1 μm particles. They
77   derived a transfer function that showed that the PMS >0.3 μm channel (CH1) response was
78   maximum at particle diameter 0.26 μm but decreased significantly below this size. They
79   concluded that the PMS behaved more like a nephelometer than an optical particle counter.
80   Kuula et al. (2020) generated monodisperse dioctyl sebacate oil droplets from 0.5 to 20 μm and
81   measured the PMS CH1 response versus particle diameter using an aerosol particle sizer (APS).
82   Their data showed that the PMS relative response decreased for particles >0.5 μm diameter.
83   Tryner et al. (2020) evaluated three low-cost particulate matter sensors, including the PMS, by
84   exposing them to five different types of aerosols in the laboratory. They found that the ratios of
85   PMS-reported to filter-derived $PM_{2.5}$ mass concentrations were inversely proportional to mass
86   median diameter (MMD). Wood smoke had the smallest MMD, 0.42 μm; its PMS $PM_{2.5}$

87   averaged 2.5 times the filter-derived $PM_{2.5}$. Conversely, oil mist had the largest MMD, 2.9 μm;
88   its PMS $PM_{2.5}$ averaged only 0.23 times the filter-derived $PM_{2.5}$.

89   Climate modeling requires a robust set of models and atmospheric measurements for predicting
90   anthropogenic aerosol radiative forcing. Currently, there are uncertainties in the modeling
91   results, due in part to the sparseness of ground-based data used to evaluate and refine the models
92   (e.g., Gliss et al., 2021). Satellite observations provide global coverage that can be used for
93   model evaluation, but satellite data require further assessment, particularly when trying to
94   provide information about surface aerosol properties. The Surface Particulate Matter Network
95   (SPARTAN) (https://www.spartan-network.org/; Snider et al., 2015) was specifically designed
96   to assess and improve algorithms to relate satellite retrievals to surface aerosols. SPARTAN
97   operates collocated filter-based $PM_{2.5}$, aerosol scattering coefficient via nephelometer, and
98   aerosol optical depth (AOD) measurements at approximately 20 sites around the world. Model
99   and satellite uncertainties can be reduced using a distributed set of low-cost sensors that can
100   provide aerosol light scattering estimates at a higher spatial and temporal resolution than is
101   possible using nephelometers alone. Low-cost sensors are increasingly being used along with
102   satellite data to estimate global aerosol impacts (Gupta et al., 2018).

103   There is ongoing scientific debate about the accuracy and precision of these low-cost sensors and
104   their limitations (Morawska et al., 2018; Jayaratne et al., 2020). Many of the recent papers
105   discuss performance evaluations or "calibrations" of these low-cost sensors by comparing their
106   measurements with traditional, research-grade aerosol measurements (Papapostolou et al., 2017;
107   Barkjohn et al., 2020). The concerns over data quality, stemming largely from inexpensive
108   components, lack of transparency of signal processing, and inadequate quality control and testing
109   at the factory, must be weighed against the advantages of low cost and wide spatial coverage.

110   The actual measurement in the PA monitor with its two PMS5003 sensors (PA-PMS), and in
111   many other low-cost aerosol monitors, is of light scattered by particles integrated over a wide
112   range of angles (Kelly et al., 2017), which has traditionally been done in atmospheric research
113   and aerosol monitoring programs using integrating nephelometers. Aerosol light scattering and
114   extinction measurements are useful in many applications, including determination of the
115   radiative forcing effects of aerosols on climate change, atmospheric visibility, wildfire/smoke
116   impacts, and validation of model outputs and satellite retrievals (e.g., Malm et al., 1994;
117   Sherman et al., 2015; Snider et al., 2015; Gliss et al., 2021). Even though most low-cost aerosol
118   sensors use light scattering as the basis of their operation, almost none have been evaluated as a
119   low-cost nephelometer to estimate atmospheric light scattering. Markowicz and Chilinski (2020)
120   conducted a 3 year evaluation of two low-cost sensors versus the Aurora 4000 polar integrating
121   nephelometer at a site in southeastern Poland. They found that the mass concentration of
122   particles with aerodynamic diameters <10 μm (PM_{10}) from the DfRobot SEN0177 and the
123   Alphasense OPC-N2 were highly correlated ($r^2 > 0.89$) with the aerosol scattering coefficient
124   measured by the nephelometer. They were able to estimate the 1 h average aerosol scattering
125   coefficient from the low-cost sensors with a root mean square error (RMSE) of 20 Mm^{-1},
126   corresponding to 27% of the mean aerosol scattering coefficient.

127   Unfortunately, due to cost, availability, and the expertise required to run them, integrating
128   nephelometers are not operated in great numbers around the world. A recent analysis by Laj et
129   al. (2020) showed 56 long-term monitoring stations reporting their nephelometer data to the

130   World Meteorological Organization (WMO) Global Atmosphere Watch (GAW) World Data
131   Centre for Aerosols. This count includes nephelometers operated in several monitoring
132   networks, including the National Oceanic and Atmospheric Administration's (NOAA) Federated
133   Aerosol Network (NFAN, Andrews et al., 2019), the Aerosols, Clouds and Trace Gases Research
134   Infrastructure (ACTRIS) network (e.g., Pandolfi et al., 2018), and the Interagency Monitoring of
135   Protected Visual Environments (IMPROVE) network (Malm et al., 1994). While there are more
136   nephelometers in use around the world for short-term field and laboratory studies, the number
137   almost certainly does not exceed a few hundred. This is small compared with the number of low-
138   cost aerosol monitors in use globally.

139   This paper presents an evaluation of the performance characteristics of the low-cost PA-PMS
140   monitor to measure the integrated aerosol light scattering coefficient. It is shown that the PA-
141   PMS sensor configuration is similar to a cell-reciprocal nephelometer. A physical-optical model
142   based on Mie theory and the PMS geometry is created that predicts scattered light intensity on
143   the PMS photodiode and aerosol forward and backward light scattering truncation. PA-PMS
144   measurements are compared to yearlong measured aerosol light scattering coefficients at
145   NOAA's Mauna Loa Observatory (MLO) in Hawaii and to measured and modeled aerosol light
146   scattering coefficients and aerosol size distribution at the Boulder Table Mountain (BOS) site in
147   Colorado. Finally, an empirical relationship is developed to estimate the submicron light
148   scattering coefficient and its uncertainty from the PA-PMS data.

149   With a better understanding of what the PA measures, how it works, and its uncertainties, the
150   large network of PA-PMSs could be used to estimate the submicrometer aerosol scattering
151   coefficient at visible wavelengths throughout the world. These data could then be used to
152   improve chemical transport and general circulation models, advance climate change predictions,
153   and provide for better air quality forecasts.

2. Instrument description

155   In this section we first describe the physical and optical characteristics of the PA-PMS to place it
156   in the context of nephelometry. We then provide a brief overview of integrating nephelometers,
157   which are instruments designed specifically to measure light scattering.

2.1 PA-PMS nomenclature

159   The PMS sensor outputs 14 fields that are processed and reported by the PA. Each of these
160   fields will be referred to as a channel. For instance, the PA-reported number concentration of
161   particles >0.3 μm is referred to as CH1 in the remainder of this paper, number concentrations
162   >0.5 μm as channel two (CH2), and so forth. Furthermore, the two PMS sensors embedded in
163   the PA will be referred to as either sensor A or sensor B. Therefore, the number concentration of
164   particles >0.3 μm derived from sensor A will be referred to as CH1A and those from sensor B as
165   CH1B. The average of CH1A and CH1B will be referred to as CH1avg. The PMS reports the
166   CH1 units as "#/dl", which is the number of particles having diameters >0.3 μm per deciliter. In
167   this paper the PMS units for CH1 are not used.

2.2 Description of the PA and its PMS 5003 sensors

169   The PA monitor integrates two PMS sensors, a Bosch BME280 pressure, temperature, and RH
170   sensor and an ESP 8266 chip (https://www2.purpleair.com/pages/technology). The PA-reported

171 temperature and RH are based on the sensor attached to the circuit board, and do not necessarily
172 represent ambient conditions. The available specifications of the PMS are incomplete, and the
173 processing algorithms are unknown (He et al., 2020). The following is based on available
174 information and, where needed, professional judgment. Each PMS includes a small laser, a
175 photodiode, a small fan to draw air across the laser beam, a microprocessor control unit (MCU),
176 and probably an operational amplifier. The MCU processes the signal from the photodiode and
177 outputs the following data fields approximately once per second: >0.3 μm, >0.5 μm, >1.0 μm,
178 >2.5 μm, >5 μm, >10 μm, PM_1, $PM_{2.5}$, and PM_{10}. The PMS denotes the first six data fields as
179 particle number concentrations above the designated cutpoint and the last three data fields as
180 mass concentrations of particles below the designated cutpoints; the PM data fields are reported
181 for two different conditions, "standard particles" and "under atmospheric environment". The PA
182 ESP8266 chip calculates 2 min averages of the PMS and BME280 signals. It transmits them
183 wirelessly and writes them as a CSV file on a micro SD card.

184 **2.2.1 Airflow and particle losses**

185 The recommended orientation of the PA results in aerosol being drawn upward by a small fan
186 through four 3 mm diameter entrance holes in each PMS. The aerosol then enters a 9.4 cm^3
187 chamber (Fig. S1a) and flows upward, parallel to and exposed to the circuit board as shown in
188 Fig. S1b. Particles then make a 180 degree turn through three exit holes at the top of the chamber
189 to emerge on the other side of the circuit board and flow downhill through a 1.1 cm^3 channel that
190 is illuminated by the laser. The total PMS volume is estimated to be 9.4 + 1.1 = 10.5 cm^3. The
191 PMS volumetric flow rate is estimated to be 1.5 $cm^3\,s^{-1}$ (~0.090 lpm) based on measurements
192 described in Supplemental Materials Sect. S1. The estimated inlet velocity through the entrance
193 holes is estimated to be 5.3 $cm\,s^{-1}$.

194 The PMS inlet orientation 90 degrees to the wind, upward flow, and the low inlet velocity
195 through the sampling holes can result in significant aspiration losses of larger particles (Hangal
196 and Willeke, 1990). Aspiration losses are greater at higher wind speeds because it is more
197 difficult for the larger particles to follow the streamlines into the low velocity PMS inlet. This
198 can result in a lower concentration of larger particles entering the PMS than are in the ambient
199 air. Particle aspiration losses are proportional to the particle Stokes number and the ratio of the
200 wind velocity to the inlet face velocity (Hangal and Willeke, 1990). More details are provided in
201 Supplemental Materials Sect. S1.

202 At typical wind velocities of 1–3 $m\,s^{-1}$, the ratio of PMS inlet face velocity to wind speed is only
203 0.02 to 0.05, much lower than typical sampling ratios of 0.5 to 6.0 (Brockman, 2011). Pawar and
204 Sinha (2020) addressed this problem for the Laser Egg low-cost sensor by putting it in a box and
205 adding a 40 lpm fan to increase the inlet-to-wind velocity ratio and to direct the airflow upward
206 to the Laser Egg inlet. During calm winds, large particle aspiration losses may occur by particle
207 gravitational settling, acting against the PMS upward flow (Grinshpun et al., 1993). The actual
208 wind conditions in the ambient air and in the PA near the PMS sample inlet are turbulent. Hangal
209 and Willeke (1990) found in their wind tunnel experiments that turbulence intensity had a
210 negligible effect on aspiration efficiency. Calculations using Eq. S1 (see Fig. S2) predict that at a
211 wind speed of 1 $m\,s^{-1}$, the PMS aspiration losses for particles >2 μm may be significant.
212 However, it must be cautioned that the literature does not include data for the very low 5.3 $cm\,s^{-1}$

213   PMS face velocity, and actual measurements of the PMS aspiration efficiencies were not made.
214   They may be significantly different from these calculated efficiencies.

215   Inside the PMS 9.4 cm^3 chamber, the air has an average velocity of 0.57 cm s^{-1} and Reynolds
216   number of 6.1, resulting in an average residence time of 6.3 s. The average air velocity in the
217   chamber is equal to the sedimentation velocity of a spherical 10 μm diameter particle with a
218   density of 2 g cm^{-3} in air at STP (standard temperature and pressure; values used in this analysis
219   are 273.15 K and 1013.25 hPa, respectively). This suggests that some 2 g cm^{-3} density particles
220   with diameters >10 μm that enter the PMS would settle out in the chamber and not make it to the
221   three exit holes at the top of the chamber. Ultrafine particles can also be lost to the walls of the
222   chamber and the printed circuit board due to convective diffusion. Calculations using the
223   equation for diffusional losses (Friedlander, 1977) show that less than 1% of the 0.01 μm
224   diameter aerosols would be lost in the chamber due to convective diffusion, with even smaller
225   diffusional losses for larger particles.

226   Loss of particles due to inertial impaction on the wall opposite the three holes (Fig. S1b) was
227   estimated by the local air flow Reynolds number near the three holes and the aerosol Stokes
228   number. The local Reynolds number is calculated to be 23, and the Stokes number for 10 μm
229   particles is 8.2×10^{-4}. At these low numbers, the calculated loss to impaction is less than 1% for
230   all particles less than 10 μm diameter (Hering, 1995).

231   The average flow velocity through the laser beam is approximately 3.0 cm s^{-1}. By the time the
232   air flows through the laser beam, it has lost most of the particles over 10 μm diameter. Further
233   particle losses due to gravitational settling over the photodiode would be very small, since the
234   gravitational force is parallel to the photodiode.

235   In summary, it is likely that the laser in the PMS is sampling a lower concentration of particles >
236   2 μm diameter than in the ambient air. Based on the literature and calculations, the dominant
237   coarse aerosol loss mechanism may be aspiration, not internal losses. However, further
238   measurements are needed to assess the various aerosol loss mechanisms.

239   **2.2.2 Laser**
240   The wavelength and power of three PMS diode lasers were measured using an Ocean Optics Red
241   Tide USB650 spectrometer and Melles Griot Universal Optical Power Meter, respectively. The
242   wavelength averaged 657 +/- 1 nm, and the power averaged 2.36 +/- 0.04 mW. The laser is
243   polarized parallel to the plane of the photodiode detector. This results in the aerosol-scattered
244   light being polarized perpendicular to the plane of incidence. Figure S3 shows that
245   perpendicular polarization results in significantly greater scattering intensity from 0.3 μm
246   particles compared to natural or parallel polarization. It is probable that many low-cost PM
247   sensors have lasers that are polarized. Polarization will affect how the sensors respond to various
248   size particles and needs to be considered when modeling sensor behavior.

249   The PMS laser beam profile is not a simple plane wave, but complex in shape. The laser has a 3
250   mm diameter lens that focuses the laser over the photodiode. The beam profile evolves
251   significantly as it goes through the focal region (Naqwi and Durst, 1990). The laser beam
252   diameter in the laser sensing region over the photodiode was not measured. It was estimated by
253   eye to be 0.5 to 1.0 mm, with significant uncertainty. The PMS MCU turns the laser on and off

254   every 800 msec or 2.5 s, depending on aerosol concentration. The laser pulses are 600–900
255   msec, with the laser power on continuously during this time. We hypothesize that the PMS MCU
256   gathers data during laser on, processes it during laser off, and uses the difference of the
257   photodiode output during these stages to obtain and subtract any electronic or stray light (other
258   than the laser) background signal to the photodiode.

259   **2.2.3 Photodiode detector**

260   The actual photodiode model in the PMS is unknown. The photodiode appearance is similar to
261   the BPW34 silicon PIN photodiode. In this paper the specifications of the BPW34 are used to
262   estimate the likely properties of the detector in the PMS. It has a very large dynamic range when
263   operated with reverse bias. The dependence of the photodiode current on the light intensity is
264   very linear over 6 or more orders of magnitude, e.g., in a range from a few nanowatts to tens of
265   milliwatts. Silicon PIN photodiodes have low dark current, a 20 nanosecond rise time, and good
266   wavelength sensitivity between roughly 400 and 1000 nm. (https://www.rp-
267   photonics.com/photodiodes.html). At a wavelength of 657 nm, the BPW34 produces
268   approximately 0.4 microampere current per microwatt of incident radiant power
269   (https://www.fiberoptics4sale.com/blogs/archive-posts/95046662-pin-photodetector-
270   characteristics-for-optical-fiber-communication). The PMS does not have any optical elements
271   to capture and focus the aerosol-scattered light on its photodiode.

272   The photodiode does not have a cosine corrector in front and is probably not a true cosine
273   detector. However, the relative spectral sensitivity is advertised to be a cosine response by the
274   manufacturers
275   (https://www.osram.com/ecat/DIL%20BPW%2034%20B/com/en/class_pim_web_catalog_1034
276   89/prd_pim_device_2219537/ and https://www.vishay.com/docs/81521/bpw34.pdf).

277   **2.2.4 Laser and photodiode geometry**

278   The PMS geometry is very similar to a cell-reciprocal nephelometer. Figure 1 shows the PMS
279   laser and photodiode geometry. The measurements were made with a Brown & Sharpe
280   micrometer. The distance from the laser exit hole to the photodiode is 2.5 mm; the perpendicular
281   distance from the center of the laser beam to the photodiode is 1.8 mm; the diameter of the
282   exposed photodiode area is 3.0 mm; the thickness of the base mask over the photodiode is 0.46
283   mm; and the distance from the edge of the photodiode to the end of the laser sensing volume is
284   4.5 mm. θ_1 is the lower angular scattering limit, and θ_2 is the upper angular scattering limit for a
285   particle in the laser.

286   Due to the PMS geometry, the upper and lower angular scattering limits for θ depend on the
287   location, x, of a particle in the laser. This can be seen in Fig. S4. For example, at x = 0 mm, at the
288   laser exit, the upper and lower scattering limits for θ are 18–38 degrees. At x = 4.0 mm, over the
289   center of the photodiode, the angular integration limits are 50–130 degrees. The PMS photodiode
290   is not capable of detecting light scattered from particles at less than 18 degrees.

291   Figures S5–S9 provide more detail about the PMS dimensions and geometry.

2.2.5 PMS5003 sensing volume

The sensing volume is the volume in which the aerosol is irradiated by the laser. The sensing volume extends the length of the laser where the aerosol flows through it, approximately 10 mm. The sensing volume is shown in Fig. S9. The average residence time of a particle in the laser beam is approximately 30 ms. Some of the scattered light is detected by the photodiode and creates a voltage pulse approximately 30 ms wide. It appears that the photodiode is detecting either a cloud of particles from the sensing volume or individual pulses, depending on the concentration. At low concentrations, the aerosol concentration within the sensing volume is unlikely to be uniform, resulting in large relative changes in output per second.

2.2.6 Signal processing and electronics

It is not reported how the PMS MCU differentiates and processes the photodiode signals. The PMS MCU sends the PA a signal approximately every second in the form of a digital sequence of unsigned 16 bit binary data words, and CH1 is thought to be proportional to the photodiode current. The photodiode current was not measured in this study. The PA creates 80 s (Firmware Version 3) or 120 s (Firmware Version 4 and higher) averages and writes them to its micro SD card. We measured an average percentage difference of 0.3% between the 2 min averages reported by the PA and the 2 min averages calculated from the 1 s values from the PMS. The results are shown in Fig. S10. It is apparent that the processing done by the PA to calculate its reported 2 min averages does not bias the results.

2.2.7 PMS CH1 variability in sampling filtered air

We found significant variability in PMS response to filtered air. We exposed 21 PAs containing 42 PMS sensors to filtered air for 2 to 94 hours. The results are summarized in Table S1. Hourly average CH1 ranged from 0.10 to 377. Eleven PAs had both PMS CH1A and CH1B averages below 2, while seven PAs had at least one CH1 average over 26. We recommend that before deployment the PAs sample filtered air for at least four hours to identify and eliminate PAs with CH1 hourly averages over 2 in filtered air. Removing PAs with high CH1 offsets in filtered air reduces uncertainty and improves precision, particularly in cleaner ambient air.

2.2.8 PMS CH1 unresponsive to CO_2 and Suva[®]

Filtered air, CO_2, and Suva[®] (DuPont™ Suva[®] 134a refrigerant) are often used to calibrate integrating nephelometers (Anderson et al., 1996). The Rayleigh scattering coefficients of filtered air, CO_2, and Suva at 657 nm and at STP (0 ℃ and 1013.25 hPa) are 5.5, 13.3, and 46.2 Mm^{-1}, respectively. We found that the PMS was unresponsive to 100% CO_2 (Fig. S11) and Suva. The CH1 for each gas was the same as filtered air. These results indicate that the PMS signal processing zeroes out a constant scattering signal and cannot be used to measure the scattering coefficient of gases that are commonly used in calibrating nephelometers. Furthermore, the method used by the PMS to subtract light scattering by air molecules in the sampling volume is unknown.

2.2.9 PMS CH1 and CH1avg precision

The PMS CH1 precision was measured by collocating ten PA monitors on the roof of the NOAA building in Boulder, Colorado, between 22 January 2021 and 1 February 2021. These monitors

332 were not checked with filtered air before deployment. It was found that two of the PMS sensors
333 had large offsets and two had moderate offsets at low CH1 values. One PMS sensor was found to
334 produce errant data and was removed from the analysis, resulting in valid data from 19 CH1A
335 and CH1B sensors in the ten PAs.

336 The precisions for the hourly data from the CH1A and CH1B sensors and their average
337 (CH1avg) were estimated as the coefficient of variation for each of the 19 CH1A and CH1B
338 values and the 9 CH1avg values for each hour, which are plotted against the average CH1 values
339 in Fig. 2. As shown, above CH1 values of 500, the precision is relatively constant with an
340 average of 8% and 4.8% for CH1A-CH1B and CH1avg, respectively. Below CH1 values of 500,
341 the uncertainties increase rapidly with decreasing CH1 values.

342 There are two mechanisms that may contribute to the rapid uncertainty increase for CH1 < 100.
343 First, it is likely that some of the increased uncertainty in CH1 below values of 100 is inherent to
344 sampling low concentrations, as is the case for any instrument. Second, the geometry of the laser
345 sensing volume in the PMS can contribute to uncertainty in the CH1 at low concentrations,
346 specifically if particles are not distributed uniformly within the laser beam.

347 The data in Fig. 2 can be modeled by the sum of squares of an additive (Un_{add}) and multiplicative
348 uncertainty (Un_{mult}) (Currie, 1968; Hyslop and White, 2008; JCGM100:GUM, 2008):

349 $$Uncertainty = \sqrt{Un_{add}^2 + Un_{mult}^2 * CH1} \qquad (1)$$

350 Equation 1 was fitted to the precision data in Fig. 2 where the Un_{mult} was set to the average
351 precision at high CH1 values, and Un_{add} was set to 28 and 19 for the A and B sensors and
352 CH1avg, respectively, to fit the highest variances (Table S2). The Un_{add} is the precision of CH1
353 as CH1 approaches zero and is assumed to be equivalent to the uncertainty in values below the
354 instrument minimum detection limit (MDL) or that of blanks (Currie, 1968), which were 0.08
355 and 0.048 for the A and B sensors and CH1avg, respectively. The coefficient of determination in
356 the model fit for both sets of data was $r^2 = 0.96$. Defining the MDL as the 99% confidence
357 interval of the Un_{add} (Code of Federal Regulations, 40 CFR 136, https://ecfr.io/Title-40/Part-
358 136), MDLs for the individual CH1 sensors and CH1avg were 65 and 44, respectively.

359 As shown in Sect. S3, the Un_{mult} and Un_{add} are highly dependent on the systematic biases
360 between the individual CH1 sensors and CH1avg and the four CH1 sensors with data offsets as
361 the CH1 approaches zero (Fig. S12). Removing these four sensors and normalizing the data for
362 each CH1 sensor by its average reduced the Un_{add} and Un_{mult} to 9% and 3%, respectively, for the
363 CH1 sensors and 6% and 1.9%, respectively, for the CH1avg data. These results correspond to
364 an MDL of 21 and 14 for the normalized CH1 sensor and CH1avg data, respectively. Based on
365 these results, an "off the shelf" PA will have a CH1avg MDL of about 44 and precision of less
366 than 4.3%, but the careful selection of a PA without an offset and that has relatively low noise
367 will have an MDL of 14 and precision of less than 1.9%.

2.3 Overview of cell-direct and cell-reciprocal nephelometers

369 The integrating nephelometer was invented during World War II (Beuttell and Brewer, 1949). It
370 provides a direct measure of aerosol light scattering integrated over a large angular range, the
371 "aerosol light scattering coefficient". This measure requires no assumptions about aerosol

372 composition, size distribution, refractive index, or shape. The most common nephelometer
373 configurations are the "cell-direct" and "cell-reciprocal". Figure 3 presents schematics of the two
374 types of nephelometers. The geometrical relationship between the laser and the photodetector in
375 the PMS resembles a cell-reciprocal nephelometer (Fig. 3b).

376 Middleton (1952) was the first to show that the cell-direct nephelometer with a Lambertian
377 (cosine-adjusted diffuser) light source directly measures the aerosol light scattering coefficient.
378 Anderson et al. (1996), following the derivation in Butcher and Charlson (1972), added
379 geometrical diagrams to make Middleton's derivation much clearer. Mulholland and Bryner
380 (1994) proved that the cell-reciprocal nephelometer with a Lambertian diffuser followed by a
381 photodiode placed at the center of the cell-reciprocal nephelometer also directly measures the
382 aerosol scattering coefficient. This put both the cell-direct and cell-reciprocal nephelometers on
383 equal theoretical footing.

384 There are a number of cell-direct nephelometers in use today. They include the TSI 3563 (St.
385 Paul, MN, USA; Anderson et al., 1996), the Ecotech Aurora Models 3000 and 4000 (Knoxfield,
386 Australia; Müller et al., 2011), the Radiance Research M903 (Seattle, WA, USA; Heintzenberg
387 et al., 2006), and the Optec NG-2 (Lowell, MI, USA; Molenar, 1997). In contrast, cell-
388 reciprocal nephelometers have more limited commercial availability. The photoacoustic
389 extinctiometer (PAX; Droplet Measurement Technologies, Inc., Longmont, CO, USA) and the
390 three-wavelength photoacoustic soot spectrometer (PASS-3) use a cell-reciprocal nephelometer
391 to measure the aerosol light scattering coefficient (Arnott et al., 2006). A cosine corrector
392 followed by a photomultiplier tube is placed at the center of the cell-reciprocal nephelometer
393 (Abu-Rahmah et al., 2006; Nakayama et al., 2015).

394 A "perfect nephelometer" is one in which the nephelometer is able to see the scattered light over
395 the entire angular range from 0 to 180 degrees. In practice, this cannot be achieved for the cell-
396 direct and cell-reciprocal nephelometers. Both the forward and backward scattering angles are
397 truncated. For example, the TSI 3563 nephelometer has measured angular truncation below
398 about 7 degrees in the forward direction and above 170 degrees in the backward direction
399 (Anderson et al., 1996; Heintzenberg and Charlson, 1996). For the PASS-3, Nakayama et al.
400 (2015) found that both the large effective truncation angle (21 degrees) as well as the
401 perpendicular polarization of the 532 nm laser relative to the scattering plane contribute to the
402 large particle size dependence of measured scattering. Light scattering from ammonium sulfate
403 particles of 0.71 μm diameter was reduced by 50% relative to a perfect nephelometer. Angular
404 truncation generally results in nephelometers underestimating the contribution of particles larger
405 than approximately 1 μm diameter to the scattering coefficient, although corrections have been
406 developed to account for angular nonidealities (e.g., Anderson and Ogren, 1998; Müller et al.,
407 2011).

3. A physical-optical model of the PMS5003

409 To gain insight into how the PMS responds to ambient aerosol properties, a model was
410 developed to estimate the intensity of scattered light impinging on the PMS photodiode. The
411 primary purpose of the model was to predict how the PMS performance compares to other
412 instruments designed to measure the aerosol scattering coefficient, such as integrating
413 nephelometers. The model makes simplifying assumptions about the laser that allow the

414   application of Mie theory to the light scattered from particles in the laser. Details of the model
415   are presented in the Appendix.

416   The equation describing the intensity of light scattered from a particle in the laser is (Middleton,
417   1952; Anderson et al., 1996)

418    $I(\theta) = F_{dv}\ \beta_p(\theta)\ dv$ (2)

419   where $I(\theta)$ is the intensity of light at angle θ scattered from a particle in the volume element dv
420   (with units of W sr^{-1}); $\beta_p(\theta)$ is the volume scattering function (m^{-1} sr^{-1}); F_{dv} is the incident laser
421   flux density (W m^{-2}) impinging on the volume element dv; and dv is the volume element within
422   the laser.

423   The volume scattering function for a single particle in the laser beam is a function of aerosol
424   diameter D_p, complex refractive index m, laser wavelength λ, and scattering angle θ:

425    $\beta_p(\theta) = (\lambda/2\pi)^2\ (1/dv)\ |S_1(m, \lambda, \theta, D_p)|^2$ (3)

426   where $|S_1(m, \lambda, \theta, D_p)|^2$ is the Mie scattering intensity function for laser light polarized parallel to
427   the photodiode surface and perpendicular to the plane of incidence (Bohren and Huffman, 1983).

428   The scattered light intensity from a single particle in the laser beam to a narrow strip across the
429   middle of the photodiode and from all positions in the scattering volume is integrated to predict
430   the total power received by the photodiode as a function of particle diameter D_p and refractive
431   index m:

432    $P(m, D_p) = K \int_{x=0}^{x=10mm} \int_{\theta_1(x)}^{\theta_2(x)} |S_1(m, \theta, D_p)|^2 \sin(\theta)\ d\theta\ dx.$ (4)

433   Due to the PMS geometry, the upper and lower angular scattering limits for θ depend on the
434   location, x, of a particle in the laser. Details are provided in the Appendix. This approach can be
435   used to estimate the amount of scattered energy detected from mixtures of particles of varying
436   diameters and indices of refraction, as shown in Eq. (5):

437    $P = K \int_{Dp} \int_{x=0}^{x=10mm} \int_{\theta_1(x)}^{\theta_2(x)} |S_1(m, \theta, D_p)|^2 \sin(\theta)\ N(D_p, m)\ d\theta\ dx\ dD_p.$ (5)

438   **3.1 Model predictions - Deviation from a perfect cosine response**

439   As discussed above, the PMS has a photodetector that is about 1.8 mm below the laser, resulting
440   in forward scattering and backscattering truncation angles of 18 and 166 degrees, respectively.
441   Furthermore, the photodetector is recessed 0.46 mm below the scattering chamber base.
442   Equation 4 is used to explore the deviation from a perfect cosine response resulting from the
443   truncated scattering volume and recessed detector. It is shown in Fig. 4. For these calculations,
444    $S_1(m, \theta, D_p)$ is set equal to 1, which corresponds to isotropic scattering or a volume scattering
445   function that is constant over all scattering angles. It is assumed that the detector has a
446   Lambertian response, i.e., the light detected is independent of the direction of the incident
447   energy, which results in a detector cosine response. Figure 4 shows a perfect cosine response in

448 yellow, while the red line shows the deviation from a perfect cosine response due to angular
449 truncation. The blue line shows the effect of both angular truncation and an inset detector that is
450 0.46 mm below the chamber base. All curves have been normalized to one at 90 degrees.

3.2 Model predictions - Intensity versus position on the detector

452 Figure 5 provides an example of the energy distribution on the photodiode as a function of
453 position in the laser and on the diode resulting from scattering from particles represented by a
454 lognormally distributed aerosol volume size distribution with a volume mean diameter of 0.33
455 µm and geometric standard deviation of 1.7. Figure 5 shows model predictions of the relative
456 intensity of scattered light, where the values are proportional to energy flux impinging on the
457 detector.

458 The masking resulting from a recessed detector truncates the scattering both in the most forward
459 and most backward scattering angles. This masking is shown as the triangular area
460 corresponding to distance down the laser and detector of 0.0–2.5 mm and 0.0–0.78 mm,
461 respectively, for the forward scattering angles and 5.6–10 mm and 1.44–3.0 mm, respectively,
462 for backscattering. Because the laser is parallel to the photodetector, which is assumed to have a
463 $\cos(90-\theta)$ response, the maximum energy scattered to the detector is approximately at $\theta = 90$
464 degrees. However, more energy is scattered to the detector for scattering angles less than 90
465 degrees, which corresponds to forward scattering, and very little energy is detected by the
466 photodiode for particles in the laser that are greater than about 8 mm down the laser beam, even
467 though the detector is exposed to particles in the laser that are 10 mm away from the laser exit
468 hole. These distances down the laser correspond to backscattering. The total energy detected by
469 the photodiode is the sum or integral across both the detector surface and position in the laser
470 and corresponds to the volume under the curve depicted in Fig. 5.

3.3 Model predictions - Predicted photodiode response as a function of particle diameter

472 The PMS differs from a perfect nephelometer in at least five important ways:
   1. The laser is polarized, whereas the nephelometer light source is unpolarized.
   2. The laser beam profile is not a simple plane wave, but complex in shape. The laser beam
    profile evolves significantly as it is focused over the photodiode.
   3. The photodiode likely does not have a perfect cosine response.
   4. The PMS geometry limits the photodiode to receiving scattered light between
    approximately 18 and 166 degrees, whereas a perfect nephelometer measures all energy
    scattered between 0 and 180 degrees.
   5. The unknown PMS signal processing removes the light scattering signal from CO_2, Suva,
    and filtered air. These gases are used to calibrate nephelometers but cannot be used to
    calibrate the PMS.

483 The effects of these differences can be seen in Fig. 6, which shows predicted photodiode
484 response as a function of particle diameter. The perfect nephelometer response is in blue, and
485 the PMS response is in yellow. The red line predicts PMS response if the laser were not
486 polarized. Relative intensities have been normalized to an ideal nephelometer measurement of a
487 0.1 µm diameter particle, which is akin to adjusting the laser power such that the scattered power
488 at a diameter equal to 0.1 µm is the same for all configurations. Scattering as a function of
489 particle diameter is nearly the same for all three configurations from 0.1 µm to about 0.3 µm. At

490 about 0.8 to 1.0 μm, the response of a PMS with an unpolarized laser is about half that of an
491 ideal nephelometer, and the use of a polarized laser reduces its response to about 30% to that of
492 an ideal nephelometer. For particles above 2 μm in diameter, the PMS response compared to an
493 ideal nephelometer is decreased by about 75%. Additionally, the PMS manual (Zhou, 2016)
494 quotes a lower detection limit diameter of 0.3 μm. The model predicts that particles smaller than
495 0.3 μm in diameter would be detected by the PMS, in direct proportion to their contribution to
496 the scattering coefficient.

497 These differences in geometry and optics from an ideal nephelometer are further highlighted in
498 Fig. 7. To highlight the effect of polarization, the blue line shows the ratio of an ideal
499 nephelometer with a laser light source that is perpendicularly polarized to an ideal nephelometer
500 with an unpolarized light source while the red line shows just the effect of PMS geometry
501 relative to an ideal nephelometer. The yellow line shows the effects that polarization and PMS
502 geometry have on the measured scattering signal. Again, all hypothetical instrument responses
503 have been normalized to a particle diameter of 0.1 μm. Relative to scattering for a 0.1 μm
504 particle, the polarization alone reduces the scattering signal of an ideal nephelometer by 40% for
505 particles with diameters in the 0.8–1.5 μm size range. The additional effect of PMS scattering
506 geometry reduces the scattering signal at 0.8–1.0 μm by about another 30% relative to an ideal
507 nephelometer.

508 As noted in Sect. 2.2.3, the specifications of the BPW34 are used to estimate the likely properties
509 of the detector in the PMS. Our model assumes two ideal properties of the photodiode. The first
510 is area uniformity - that a photon impinging any part of the photodiode would generate the same
511 current as the same photon impinging on another part of the photodiode. The second ideal
512 assumption is that the dependence of the photodiode current on the light intensity is very linear
513 over 4 or more orders of magnitude. If these assumptions do not hold, then the yellow curve in
514 Fig. 7 will change.

515 The variance in the PMS physical and optical geometry and errors in the measurements are not
516 known but likely small. To evaluate the sensitivity of the modeled PA scattering to errors in
517 these measurements, the model was exercised with large deviations of ±25% and ±50% in these
518 inputs. As shown in Table S3, the errors tend to increase with particle size. The modeled PA
519 scattering to a perfect nephelometer is most sensitive to errors in the distance from the laser to
520 the photodiode. For particle diameters of 0.5 μm, +25% and +50% changes in this distance
521 resulted in maximum differences of 10% and 20%, respectively. Based on these results and the
522 fact that the errors in the physical dimensions are less than 25%, these errors are thought to have
523 a small contribution to the overall modeled PA scattering error and were not directly accounted
524 for in the analysis. This analysis does not attempt to account for the possibility that the laser
525 beam profile is not a simple plane wave or that the laser beam profile may evolve significantly as
526 it is focused over the photodiode, and the standard plane wave Mie calculations would no longer
527 apply.

3.4 Model predictions – Differentiating by particle size

529 The irradiance received by the PMS photodiode from a particle of a given diameter and
530 refractive index depends on the particle's location in the laser beam. The model predicts that
531 particles of different sizes may contribute the same irradiance to the photodiode, depending on

532   their location in the beam, or conversely, light scattered by a particle of a given size can vary by
533   more than an order of magnitude.

534   As an example, the model predicts that all of the particles in Fig. 8 contribute the same irradiance
535   to the PMS photodiode. The smaller particles contribute the same irradiance by scattering in the
536   more effective forward scattering regime. The larger particles contribute the same irradiance by
537   scattering in the less effective backscattering regime. The photodiode and its associated
538   electronics would not be able to differentiate between them. As a result, the model predicts that
539   the values reported in the six PA-PMS particle size channels from >0.3 μm to >10 μm cannot
540   correctly represent the aerosol size distribution.

4. Experimental – Field studies

541

542   Field experiments were conducted at two of the NFAN aerosol monitoring stations: the Mauna
543   Loa Baseline Observatory in Hawaii and the Table Mountain Test Facility in Colorado. Both
544   sites have large suites of aerosol instrumentation and daily access for scientists and technicians to
545   inspect, calibrate, and maintain the instruments. These sites also have integrating nephelometers
546   (TSI 3563, St. Paul, MN, USA) against which to evaluate the PA monitors.

4.1 Description of Mauna Loa site

547

548   The Mauna Loa Baseline Observatory (MLO) is located on the north flank of the Mauna Loa
549   volcano, on the Big Island of Hawaii (19.536 ºN, 155.576 ºW, 3397 m asl). The observatory is a
550   premier atmospheric research facility that has been continuously monitoring and collecting data
551   on global background conditions and atmospheric change since the 1950s
552   (https://www.esrl.noaa.gov/gmd/obop/mlo/). Continuous aerosol measurements at MLO began in
553   the mid-1970s with the installation of condensation particle counters and an integrating
554   nephelometer (Bodhaine and Mendonca, 1974; Bodhaine et al., 1981). MLO lies above the
555   strong marine temperature inversion layer present in the region, which separates the more-
556   polluted lower portions of the island atmosphere in the marine boundary layer from the much
557   cleaner free troposphere. MLO experiences a diurnal wind pattern (Ryan, 1997) that is strongly
558   influenced by the daily heating and nighttime cooling of the dark volcanic lava rock that makes
559   up the mountain. This "radiation wind" brings air up from lower elevations during the daytime,
560   when atmospheric measurements reflect the local mountain environment. In contrast, during the
561   nighttime, downslope winds develop, and the measurements at MLO are typically dominated by
562   clean, free-tropospheric conditions (Chambers et al., 2013). At these times, the aerosol
563   measurements at MLO often reflect some of the cleanest conditions at any station in the northern
564   hemisphere. It has long been known, however, that episodic long-range transport of Asian
565   pollution and dust aerosols occurs, most frequently in the springtime (Shaw, 1980; Miller, 1981;
566   Harris and Kahl, 1990), and these aerosol events can influence both the daytime and nighttime
567   measurements at MLO. Consequently, the aerosol levels at MLO vary over a large range, from
568   extremely low to at times mildly elevated. Here we use observations from the MLO integrating
569   nephelometer to evaluate the PMS sensor.

4.2 Description of Boulder Table Mountain site

570

571   The Table Mountain Test Facility (BOS) is a large restricted-access federal complex located 14
572   km north of Boulder, Colorado (40.125 ºN, 105.237 ºW, 1689 m asl). NOAA conducts
573   atmospheric research at this site, and in addition to its NFAN station, it is one of the Global

574   Monitoring Laboratory's seven U.S. Surface Radiation Network (SURFRAD) sites
575   (https://www.esrl.noaa.gov/gmd/grad/surfrad/tablemt.html). Many instruments for measuring
576   surface and column aerosol properties are maintained at this location and used for long-term
577   monitoring of the atmosphere.

578   The BOS site lies just east of the Front Range foothills of the Rocky Mountains and is typical of
579   a semi-arid, high plains environment. It is a high mesa of predominantly grassland with some
580   desert scrub vegetation. The location is well suited for sampling of wildfire smoke plumes during
581   fire season in the western United States (summer and autumn), dust events at any time of the
582   year, and occasional urban pollution episodes. The NFAN station at BOS
583   (https://www.esrl.noaa.gov/gmd/aero/net/bos.html) was completed in September 2019. BOS
584   operates an integrating nephelometer and a differential mobility particle spectrometer (DMPS).
585   Both provided useful data for evaluating some of the predictions from the physical-optical model
586   we developed for the PMS sensor.

587   4.3 PA monitors

588   PA-PMS monitors were installed on the aerosol towers at the MLO and BOS stations, just below
589   the main aerosol inlets. MLO had two PA-PMS monitors, one gently heated and one unheated,
590   whereas BOS had one gently heated PA-PMS monitor. Prior to deployment, the monitors were
591   tested in a filtered air chamber for 4 hours to ensure that the 1 h average CH1 values were less
592   than 1 when no particles were present. One of the PMS sensors in the unheated MLO PA had 1 h
593   average CH1 values of 27 when no particles were present. The heated monitors were wrapped
594   with heating tape and powered by small DC power supplies. All the monitors were covered with
595   stainless steel flashing 5 cm below the bottom to prevent rain and snow from entering the inlet
596   (Fig. S13).

597   The PA-PMS monitors were warmed in an effort to reduce the sample RH to be closer to that of
598   the nephelometer, which is unavoidably heated to above ambient temperatures by the warmth of
599   the laboratory and by the nephelometer's halogen lamp. Because of this warming, the RH inside
600   the nephelometers rarely exceeded 40%. Both MLO and BOS are low-RH environments under
601   normal conditions, although occasionally moist air masses are encountered. The heating of the
602   monitors increased the sample temperatures by 5–8 ºC, which helped to lower the sample RH.
603   While the PA heating was not controlled to achieve an RH match with the nephelometer, it
604   brought the sample RH of the two measurements closer together. The gentle warming of the
605   heated PA to only a few degrees above ambient is unlikely to cause the PVC to off-gas or melt.
606   Heating from direct sunlight may have had a larger impact.

607   Due to internet protocols at both sites, PA's wireless data transmission feature was not used, and
608   the data were stored on the internal micro SD card. At approximately 1 month intervals, the data
609   were downloaded from the micro SD cards, and the PAs were returned to service. Outputs from
610   the two PMS sensors were then compared at these intervals to determine if the PAs were still
611   functioning properly. In this study, the 80 s or 2 min averages were used to create 1 h averages to
612   compare the PA observations to those of the nephelometer and the DMPS.

4.4 Integrating nephelometer

The integrating nephelometer (TSI Inc., model 3563) measures the aerosol light scattering coefficient at three wavelengths (450, 550, and 700 nm). At both sites, the sample flow path is switched every 6 min between 1 and 10 μm aerodynamic diameter, multijet, Berner-type impactors. Here, the scattering coefficients at 550 nm for both the PM_1 and PM_{10} size fractions are used for comparison with the PMS measurements. These are referred to as b_{sp1} and b_{sp10}, respectively.

There are two quality checks of the nephelometer operation made in the field. First, the nephelometer automatically samples filtered air once per hour. This provides a record of the stability of the instrument background measurement. Second, the nephelometer calibration is manually checked on a monthly basis using CO_2 and filtered air (Anderson et al., 1996). The 1 h average b_{sp1} in filtered air is 0.01 Mm^{-1} with a standard deviation of 0.12 Mm^{-1}, based on 125 hours of sampling filtered air.

The nephelometer measurements were corrected for angular truncation (Anderson and Ogren, 1998) and reported at STP. Weekly data review provides quality assurance of the nephelometer data. Scattering coefficient data were averaged to 1 min resolution for logging and were further averaged to hourly resolution for comparison with the PA data. The 1 h average b_{sp1} uncertainties of the nephelometer measurements are ~0.13 Mm^{-1} for scattering coefficients less than 1.0 Mm^{-1} and ~10% for scattering coefficients greater than 1 Mm^{-1} (Sherman et al., 2015).

4.5 Differential mobility particle spectrometer (DMPS)

The DMPS was provided by the Institute for Atmospheric and Earth System Research, University of Helsinki, Finland. It was checked and calibrated by the World Calibration Centre for Aerosol Physics (WCCAP) at Leibniz Institute for Tropospheric Research (IfT), Leipzig, Germany, just prior to deployment at NOAA's Table Mountain site. After shipment from IfT to NOAA, the DMPS was again checked by aerosolizing polystyrene latex spheres and confirming that the peaks occurred in the correct size bins. The DMPS was housed inside the same building as the nephelometer at BOS and sampled aerosols through the same inlet, although the DMPS flow did not pass through the aerosol impactors.

The DMPS provides 40 channels of particle concentration versus size, ranging from mobility diameters of 0.01 μm to 0.8 μm. The 0.1 μm to 0.8 μm channels of the DMPS were used to calculate hourly average fine aerosol scattering coefficient distributions and the total fine aerosol scattering coefficient, assuming spherical particles (Mie theory) with a refractive index of 1.53+0.017i. The hourly average, DMPS-calculated fine aerosol scattering coefficients were compared to the nephelometer-measured fine aerosol scattering coefficients to check operational consistency (Fig. S14). No operational changes were made to the DMPS during this field study. This study did not measure coarse aerosol size distributions. The DMPS hourly average fine aerosol scattering coefficient distributions were used with the PMS physical-optical model to predict total 1 h average scattered irradiance on the photodiode.

5. Results

This section describes our evaluation of the PA-PMS using field data from MLO and BOS. First, we provide an overview of the observational data. We then assess how well the model described

654   in Sect. 3 is able to represent the observed data and show consistency with results previously
655   reported in the literature. Next, we present results showing the potential of the PA-PMS to
656   perform as a nephelometer. Finally, we note how the size information output by the PA is not
657   correct due to the PA's primary measurement being a scattering measurement. For the results
658   presented below, data from the PA-PMS, nephelometer, and DMPS were averaged to hourly
659   frequency and merged prior to analysis.

660   **5.1 Field data overview**

661   Heated PA monitors were deployed at the MLO and BOS observatories for 15 and 11 months,
662   respectively (Table 1). At both sites weather had no impact on the operation of the PA
663   instrument, and downtime only occurred during data downloading.

664   These two deployments provide an excellent dataset for assessing PA performance in both a
665   clean location (MLO) and in an environment with more elevated particle concentration (BOS).
666   As shown in Table 2, during the field study at MLO, the median CH1 was 26.7. The median b_{sp1}
667   was 0.76 Mm^{-1} at 550 nm, which is approximately 10% of Rayleigh scattering at the MLO
668   altitude. The reported $PM_{2.5}$ mass concentration from the PA was zero for most of the MLO
669   deployment. The CH1 and b_{sp1} are adjusted to STP in Table 2. The air quality at BOS was less
670   pristine than at MLO and is more representative of nonurban continental air quality. The very
671   high maximum CH1 and b_{sp1} at BOS reported in Table 2 occurred during smoke events in the
672   summer and autumn of 2020. One of the BOS PMS sensors experienced approximately 10%
673   degradation in sensitivity after one year in the field (Fig. S15).

674   **5.2 Relationship between model predictions and field data**

675   The PMS sensor is described by the manufacturer as a particle counter that measures particles
676   between 0.3 μm and 10 μm in six size bins. Based on the theoretical characterization of the PMS
677   sensor described in Sect. 3, the sensor is more akin to a polarized, reciprocal integrating
678   nephelometer than a particle counter. Below, the field data and theoretical model are used to
679   demonstrate that the raw PMS CH1 sensor signal is an integrated scattering measurement that is
680   sensitive to particles smaller than 0.3 μm but relatively insensitive to particles larger than 1.0
681   μm.

682   **5.2.1 Predicted photodiode irradiance versus CH1 field data at BOS**

683   Our model described in Sect. 3 and the Appendix predicts a value proportional to the scattered
684   irradiance impinging on the PMS photodiode as a function of particle diameter and
685   concentration. This was done using the DMPS size distribution data from BOS. The modeled
686   PMS photodiode output is plotted against the PMS CH1 output (Fig. 9). The predicted
687   photodiode output is linearly correlated with the ordinary least squares (OLS) regression ($r^2 =$
688   0.90, normalized root mean square error (NRMSE) ~25%) with CH1 over 4 orders of magnitude.
689   The RMSE contains contributions of errors from the model-predicted radiant power, the
690   measured SMPS data the model is based on, as well as in the CH1 measurements. This strong
691   correlation and low RMSE is convincing evidence that the model and SMPS data describe the
692   PMS response quite well.

693   The linear relationship between CH1 and modeled photodiode response suggests the likelihood
694   that the CH1 output is directly related to what the photodiode is sensing (i.e., scattering from all

695 particles in the scattering volume). The PA-PMS reported values, such as concentrations of
696 particle numbers in various size ranges or PM concentrations, are quantities derived from the
697 scattering signal and the use of an undescribed algorithm.

5.2.2 Predicted aerosol size truncation versus published laboratory data

699 The PMS physical-optical model described in Sect. 3 predicts that if CH1 is proportional to the
700 photodiode power, then its signal will be reduced relative to a perfect nephelometer. Thus, the
701 ratio $CH1/b_{sp}$ should decrease as median scattering diameter increases. To test this prediction,
702 data were obtained from published laboratory studies evaluating the PMS against aerosols of
703 varying composition and size distribution reported by Tryner et al. (2020) and He et al. (2020).
704 These reported aerosol size distributions were used here to calculate the aerosol scattering
705 coefficient distributions from 0.1 to 10 μm for the various aerosols and refractive indices at a
706 wavelength of 657 nm. The median scattering diameter (MSD) was calculated for each test. The
707 MSD is the aerosol diameter at which approximately half of the light scattering coefficient is due
708 to particles smaller than the MSD and the other half to particles larger than the MSD. The MSD
709 was then compared to the ratio of the measured CH1 and b_{sp10} values, i.e., $CH1avg/b_{sp10}$, for each
710 of the tests reported in Tryner et al. (2020) and He et al. (2020). Figure 10 summarizes the
711 results for $CH1/b_{sp10}$ versus MSD.

712 The controlled laboratory results are in general agreement with the PMS physical-optical model,
713 showing substantial reduction in $CH1avg/b_{sp10}$ as a function of increasing particle diameter from
714 0.2 to 1μm. The laboratory results show an even greater reduction in $CH1avg/b_{sp10}$ than the
715 model predicts at diameters larger than 1 μm. This suggests the possibility of supermicron
716 aerosol loss before laser detection, perhaps due to aspiration as discussed in Sect. 2.2.1.

5.2.3 $CH1avg/b_{sp1}$ as a function of median scattering diameter

718 Although ambient aerosols may vary considerably in composition and morphology and cannot be
719 as simply characterized as laboratory aerosols, it is instructive to evaluate if PMS angular
720 truncation can be observed using field data. The DMPS data from BOS were used to calculate
721 hourly average aerosol scattering coefficient distributions for diameters between 0.1 μm and 0.8
722 μm. A wavelength of 657 nm and a particle refractive index of 1.53+0.0i were used for the
723 calculations. The median scattering diameter was calculated for each hour. The MSD was then
724 compared to the ratio of the measured CH1 and b_{sp1} values, i.e., $CH1avg/b_{sp1}$, for each of these
725 hours. The results are shown in Fig. 11 as a box and whisker plot of the $CH1avg/b_{sp1}$ values
726 found in each MSD bin. The center MSD value for each bin is based on a logarithmic scale of
727 MSD values where the upper and lower bin values are selected as $MSD_i+MSD_{i+1}/2$ and MSD_i-
728 $MSD_{i-1}/2$ and i refers to the ith bin. The thin black horizontal lines correspond to the number of
729 observations in each bin and the scale is shown on the right hand axis. There are less than 20
730 values in the 0.22 μm, 0.63 μm, 0.71 μm, and 0.79 μm bins. Approximately 67% of the MSDs
731 observed at BOS were between 0.29 μm and 0.36 μm, and 98% of MSDs were between 0.26 μm
732 and 0.46 μm. The overall average $CH1avg/b_{sp1}$ ratio, based on 6777 observations, is 65 Mm.

733 Figure 11 is consistent with the PMS physical-optical model. The highest $CH1avg/b_{sp1}$ ratios
734 tend to occur for aerosols with the lowest MSD and decrease as MSD increases. Additionally,
735 the results show, as suggested above, that the PMS can detect particles below 0.3 μm in diameter
736 in proportion to their contribution to the scattering coefficient.

5.2.4. Estimating the scattering coefficient minimum detection limit of the PA-PMS

The precision analysis in Sect. 2 indicates that the PA monitors used in this study estimated 1 h average CH1 and CH1avg MDLs of approximately 21 and 14, respectively. The estimated 1 h average MDL b_{sp1} of the TSI 3563 nephelometer is approximately 0.20 Mm^{-1}, based on filtered air tests. Further analysis of the relationship between CH1 and b_{sp1} at low levels was performed by plotting the ratio, CH1avg/b_{sp1}, for the combined MLO and BOS dataset, as a function of b_{sp1}. This relationship is shown graphically in Fig. 12. The data values were first averaged over 6 hours because hourly b_{sp1} values near zero included many small negative b_{sp1} values due to the very clean conditions occasionally observed at MLO. The averaging eliminated all but five negative b_{sp1} values, which were removed from the dataset. The CH1avg/b_{sp1} and b_{sp1} values were further averaged over six data points after sorting the data on b_{sp1} levels to more clearly show the relationship between CH1avg and b_{sp1}. At $b_{sp1} > 5$ Mm^{-1}, the CH1avg/b_{sp1} ratio is relatively constant at 67 Mm, the yellow line in Fig. 12. The yellow line is the slope of CH1avg versus b_{sp1} at b_{sp1} values greater than 5 Mm^{-1}. The CH1avg/b_{sp1} ratio systematically decreases from its highest values to about 35 Mm, the slope of CH1avg versus b_{sp1} at $b_{sp1} = 0.4$ Mm^{-1}. For $b_{sp1} < 0.4$ Mm^{-1} the CH1avg/b_{sp1} ratio then increases significantly as b_{sp1} decreases, consistent with CH1avg values staying approximately constant below 0.4 Mm^{-1}. Both the CH1avg and b_{sp1} are below MDL for $b_{sp1} < 0.2$ Mm^{-1}. A CH1avg/b_{sp1} ratio of approximately 35 Mm at $b_{sp1} = 0.4$ Mm^{-1} and a CH1avg value of about 14±5 is consistent with the estimated CH1avg MDL of 14.

Based on these results, the 1 h average CH1 sensor MDL for hourly data in units of scattering is approximately 0.4 Mm^{-1} at MLO. Laboratory tests challenging the PAs with known low-level, spiked aerosol concentrations and defined size distributions are needed to further refine the estimated MDL.

5.2.5 Evaluating the use of the PA-PMS as an integrating nephelometer

The MLO and BOS hourly average CH1avg are plotted against b_{sp1}, measured at 550 nm, in Fig. 13. Also shown in Fig. 13 is an OLS regression line with the intercept set equal to zero using the BOS and MLO combined dataset but with values associated with b_{sp1} less than 0.4 Mm^{-1} and greater than 500 Mm^{-1} removed. Results of the regression for the combined datasets as well as for the individual BOS and MLO datasets are presented in Table 3. There is good agreement for both datasets (Table 3) with an r^2 of 0.97 and 0.85 for the BOS and MLO datasets, respectively, and 0.97 for the combined datasets. The relationship deviates somewhat from linear with increasing slopes and scatter at lower values of atmospheric scattering coefficient, particularly for the MLO data. The slopes (in Mm^{-1}) for all data, MLO, and BOS, are $0.015 \pm 2.07 \times 10^{-5}$, $0.017 \pm 5.72 \times 10^{-5}$, and $0.015 \pm 2.68 \times 10^{-5}$, respectively. In the following analysis, a PA-derived atmospheric scattering ($b_{sp1,PA}$, Mm^{-1}) for both MLO and BOS is estimated using $b_{sp1,CH1} = 0.015 \times$ CH1avg at a wavelength of 550 nm. The best-fit value of 0.015 Mm^{-1} corresponds to the yellow horizontal line in Fig. 12 of 67.0 (1/0.015) and corresponds to a median scattering diameter of about 0.33 μm (Fig. 11).

Figure S16 shows that the submicron aerosol scattering coefficients at 550 nm and 700 nm are highly correlated, with the 700 nm scattering coefficient averaging 52% of the 550 nm scattering coefficient. This results in $b_{sp1,CH1} = 0.0078 \times$ CH1avg at a wavelength of 700 nm.

778 As discussed above, the regression coefficient between b_{sp1} and CH1 for the combined dataset of
779 0.015 Mm^{-1} is used to estimate the $b_{sp1,PA}$ derived from the CH1 channel. The data for each
780 dataset and the combined dataset were binned into ten bins based on measured b_{sp1} levels that
781 ranged from 0.4 Mm^{-1} to 500 Mm^{-1}. Values of b_{sp1} above 500 Mm^{-1} were removed from the
782 dataset. For each bin the NRMSE between $b_{sp1,PA}$ and measured b_{sp1} was calculated. The
783 NRMSE values as a function of the b_{sp1} bins are plotted in Fig. 14 for the combined dataset
784 represented as the gray bars and BOS and MLO represented by blue and orange bars,
785 respectively.

786 For b_{sp1} levels less than 0.8 Mm^{-1}, the NRMSE is 45–55%, and for b_{sp1} levels greater than 10
787 Mm^{-1}, the NRMSE is about 25% or less. For b_{sp1} levels greater than 60 Mm^{-1}, the NRMSE
788 approaches 15%.

789 As discussed in Sect. 2.2.9, the uncertainty for high CH1avg values is small (1.9% to 4.8%). The
790 precision of the TSI 3563 nephelometer is also similarly high, and together they account for
791 about 10% NRMSE at high b_{sp1} values.

792 The overall normalized error is likely due to a variety of sources, primarily the variability in the
793 CH1 values due to using a polarized light source and truncation errors due to the geometry of the
794 PA-PMS sensors. Also, the variability in aerosol characteristics such as size distribution,
795 refractive index, and shape may be important. At extremely low levels, uncertainty may also be
796 due to a nonuniform distribution of particles in the PMS laser beam.

797 There are two reasons why the PA-PMS MDL and RMSE values reported in our study are
798 surprisingly low. The TSI 3563 nephelometer has an extremely low detection limit of 0.20 Mm^{-1},
799 which is approximately 1% of Rayleigh scattering. Second, the PA-PMS has very low noise at
800 zero aerosol concentration. If the PA in our study had been collocated with a nephelometer that
801 was not as sensitive as the TSI 3563 in a location having an average fine aerosol coefficient of,
802 say, 30 Mm^{-1}, then the PA 1 h average MDL could have been significantly higher than the 0.4
803 Mm^{-1} we obtained in our study.

804 **5.2.6 PA-PMS size distributions**
805 The aerosol number concentrations from the six PMS size channels are unrealistic. The BOS
806 field data showed that the concentration of particles larger than 0.3 µm diameter calculated from
807 the DMPS averaged 10 times higher than CH1 (Fig. S17). The other PMS size channels are so
808 highly correlated with CH1 that they provide no additional information (Table S4). Furthermore,
809 it appears that the PMS creates an approximately invariant normalized aerosol number
810 distribution across a wide range of sites (Table S5, Fig. S18). Although the overall CH1
811 concentration can vary over 6 orders of magnitude (column 3 in Table S5), the shape of the PMS
812 size distribution remains fairly constant.

813 In our study, we found that the ambient aerosol size distributions measured with the SMPS
814 varied considerably at Table Mountain, as seen in Fig. 11, while the Plantower normalized
815 reported size distribution changed very little. Invariant Plantower size distributions were also
816 observed during controlled laboratory studies (He et al., 2020; Kuula et al., 2020; Tryner et al.,
817 2020). This suggests that the values in the channels above CH1 are software generated and
818 indicates that the most relevant output from the PMS is from the CH1 channel. The bottom row

819 of Table S5 shows that the PMS bin fractions above 1 µm increased by only a factor of 2–5 in a
820 high-PM$_{2.5}$ windblown dust episode at Keeler, California. This is consistent with the PMS model
821 prediction that PMS coarse aerosol response is small relative to a perfect nephelometer.

822 The results above indicate that CH1 is the primary source of aerosol information from the PMS
823 sensor. Additionally, consistent with the sensor behaving like a cell-reciprocal nephelometer, it
824 was found that CH1 was proportional to the aerosol scattering coefficient, not the number
825 concentration of particles having diameters greater than 0.3 µm. CH1 was approximately a
826 factor of 10 lower than the DMPS number concentration for a similar size range.

5.2.7 Relationship between CH1 and PM$_{2.5}$

828 The PM$_{2.5}$ mass concentration was not measured by Federal Reference Method (FRM) or Federal
829 Equivalent Method (FEM) instruments at MLO and BOS during this study. Consequently, the
830 PA-PMS PM$_{2.5}$ or CH1 results cannot be compared with PM$_{2.5}$ concentrations, but they can be
831 compared with measured scattering coefficients and discussed in the context of mass scattering
832 efficiency, which ties scattering coefficient to mass concentration.

833 Figure S19 shows that the PA-PMS PM$_{2.5}$ channel is reasonably well correlated with b$_{sp1}$ for
834 values greater than about 10–20 µg m^{-3}, typical of many moderately polluted locations, with a
835 calculated mass scattering efficiency of approximately 2.5 m^2 g^{-1}. This value of the mass
836 scattering efficiency is at the low end of the range of values reported by Hand and Malm (2007),
837 which could reflect the nature of the observed aerosols or an error of the PA-PMS PM$_{2.5}$ mass
838 concentration. This suggests that the effectiveness of the PA-PMS to serve as a PM$_{2.5}$ mass
839 concentration monitor is due both to the sensor behaving like an imperfect integrating
840 nephelometer and to the mass scattering efficiency of ambient PM$_{2.5}$ aerosols being roughly
841 constant with values in the 2–4 m^2 g^{-1} range. However, it is likely that the PA-PMS
842 underestimates PM$_{2.5}$ for very clean areas where b$_{sp1}$ is often less than 10 Mm^{-1}. For example, the
843 PA-PMS PM$_{2.5}$ was zero for 1099 of the hours in this study when b$_{sp1}$ was greater than 1 Mm^{-1}.

844 One may obtain a lower bound estimate of the PA-PMS RMSE 1 h average mass concentration
845 from the study results. Figure 14 shows the PurpleAir scattering coefficient RMSE as a function
846 of the measured scattering coefficient. For example, the PurpleAir NRMSE is 20% for a fine
847 aerosol scattering coefficient of 25 Mm^{-1}. For an aerosol having a mass scattering efficiency of
848 2–3 m^2 g^{-1}, this is approximately 10 µg m^{-3}. Thus, the PurpleAir 1 h average RMSE is roughly 2
849 µg m^{-3}. This is somewhat lower than the reported mean absolute error of ~4 µg m^{-3} for hourly
850 average PM$_{2.5}$ in Pittsburgh (Malings et al., 2020). This error assumes that the mass scattering
851 efficiency is fixed and known. This is generally not the case, and the actual error in the mass
852 concentrations will be larger.

853 The mean 1 h average fine aerosol scattering coefficient b$_{sp1}$ at MLO during our yearlong study
854 was 1.50 Mm^{-1}. From Fig. 14, the PurpleAir had a RMSE of 0.60 Mm^{-1}. For an aerosol having a
855 mass scattering efficiency of 2–3 m^2 g^{-1}, this corresponds to a 1 h average RMSE of roughly 0.2–
856 0.3 µg m^{-3}. This is well below the advertised 1 h average MDL of commercial PM$_{2.5}$ monitors.
857 For example, the BAM 1020 specifies a typical hourly detection limit of 3.6 µg m^{-3}.

6. Summary, discussion, and future work

We have demonstrated that the PMS sensor inside the PA monitor (PA-PMS) appears to behave as an imperfect reciprocal integrating nephelometer. As a scattering sensor, the PMS cannot directly count nor size particles in the air stream. The PMS uses an unknown algorithm to convert the scattering signal to a near-constant normalized number distribution from which PM concentrations are derived.

The scattering coefficient that is measured by an ideal integrating nephelometer does not need correction for any aerosol attributes such as shape, chemical composition, refractive index, or diameter. It is a valuable measure for visibility and global climate monitoring. Simple low-cost sensors such as the PA-PMS can play a role in estimating aerosol scattering coefficients and improving global coverage. Yearlong field data at NOAA's Mauna Loa Observatory and Boulder Table Mountain sites show that the 1 h average of the PA-PMS CH1 is highly correlated with a nephelometer-measured fine aerosol scattering coefficient at 550 nm, b_{sp1}, over a wide scattering coefficient range of 0.4 Mm^{-1} to 500 Mm^{-1}. The relationship between CH1 and b_{sp1} at 550 nm is found to be b_{sp1} (Mm^{-1}) = 0.015 × CH1 when both quantities are adjusted to the same temperature and pressure.

The physical-optical model developed in this paper for the PMS and the general consistency with both published laboratory data for a variety of fine aerosols and ambient field data may motivate users of other low-cost sensors to develop similar models. It is possible that some of the other low-cost sensors also use polarized lasers in a cell-reciprocal configuration like the PMS. Such models would improve the understanding of sensor operation and help users better recognize the opportunities and limitations of other low-cost sensors in applications such as monitoring the scattering coefficient.

The strong relationship between b_{sp1} and CH1 and the general agreement between the model and published laboratory data support characterizing the PA-PMS as an imperfect truncated cell-reciprocal nephelometer. The results demonstrate that it is possible to use the PA-PMS to estimate the 1 h average fine aerosol scattering coefficient across a wide range of aerosol scattering concentrations, provided the aerosol median scattering diameter is between 0.26 μm and 0.46 μm. The CH1 and b_{sp1} relationship is dependent on the size distribution, and it is expected to change for locations and times where the particle size shifts to larger or smaller sizes than those measured at BOS and MLO.

We found that the PA-PMS has important limitations compared to integrating nephelometers. It measures the light scattering over a smaller angular range, causing a significant truncation of the scattering signal in the forward and backward directions. Additionally, the PA-PMS uses a polarized light source; the sensor most likely does not have a cosine response; the laser beam profile is not a simple plane wave; and the inlet/geometry creates a broad uncertain particle size cut point. Nephelometers calibrate their scattering coefficient with CO_2 or Suva, but the PMS is unresponsive to these gases. As a result, there is currently no convenient way to calibrate the PMS to ensure its accuracy. Neither PA nor Plantower provide technical support. Quality assurance and control are not as robust as one encounters for regulatory and scientific monitoring instruments. For this reason, it is useful to test the PMS sensors in filtered air before using them and to limit field use to those sensors that have 1 h average CH1 values less than 2. While

900   sampling, it is necessary to compare 1 h averages from the two PMS sensors in each PA monitor
901   to become aware of any changes and, if needed, to replace them in a timely fashion.

902   This study limited its findings to low-RH air, because both the PA monitors and the
903   nephelometers were heated to reduce RH. Since RH plays such an important role in water uptake
904   by hygroscopic aerosols and the concomitant increase in the scattering coefficient, future work is
905   planned to compare unheated PA monitors with an unheated nephelometer that does not reduce
906   RH before sampling. Our model predicts that the PMS may not be as responsive to hygroscopic
907   growth as an unheated nephelometer. This is a topic of current study.

908   The PA-PMS reports a mass concentration of $PM_{2.5}$ particles, and many papers have been written
909   to compare the PA-PMS values with reference instruments and explain the observed differences.
910   The modest agreement that has been reported is the direct result of two factors generally
911   overlooked in those publications: the PA-PMS behaves like an imperfect integrating
912   nephelometer that provides a representative value of the light scattering coefficient, and the mass
913   scattering efficiency of $PM_{2.5}$ aerosols is roughly constant, with values in the 2–4 m^2 g^{-1} range.

Appendix

915   The PMS physical-optical model makes some simplifying assumptions. The actual PMS laser
916   beam profile is not a simple plane wave but complex in shape. The model assumes the laser is a
917   plane wave with a constant laser beam irradiance profile. This allows the use of Mie theory to
918   predict the light scattered by particles in the laser. Secondly, the model calculates the light
919   scattered to a narrow strip across the middle instead of the entire photodiode. It assumes that the
920   irradiance received by the narrow strip is representative of the entire photodiode.

921   The intensity of light scattered from a particle in the laser is

922      $I(\theta) = F_{dv}\, \beta(\theta)\, dv$ (A1)

923   where $I(\theta)$ is the intensity of light at angle θ scattered from a particle in the volume element dv
924   (with units of Watt sr^{-1}); $\beta(\theta)$ is the volume scattering function (m^{-1} sr^{-1}); F_{dv} is the incident laser
925   flux density (Watt m^{-2}) impinging on the volume element dv; and dv is the volume element
926   within the laser.

927   The volume scattering function for a monodisperse aerosol having a diameter D_p and number
928   concentration $N(D_p)$ in the PMS laser is

929      $\beta(m, \lambda, \theta, D_p) = (\lambda/2\pi)^2\, N(D_p)\, |S_1(m, \lambda, \theta, D_p)|^2$ (A2)

930   where $|S_1(m, \lambda, \theta, D_p)|^2$ is the perpendicular scattering intensity function; λ is the laser
931   wavelength; m is the particle complex refractive index; θ is the scattering angle; and D_p is the
932   aerosol diameter. Note that $\theta = 0$ in the direction of the laser, and $\theta = 90$ degrees perpendicular to
933   the laser and photodiode.

934   For one particle of size Dp in the volume element dv, $N(Dp)\, dv = (1/dv) \times (dv) = 1$.

935 The incremental power dP (Watt) scattered from a particle in the volume element dv across a
936 solid angle $d\Omega$ subtended on the surface of a sphere at distance r from the particle, and normal to
937 r, is

938 $dP = I(\theta)\, d\Omega$. (A3)

939 $d\Omega = dA_0 / r^2$, where dA_0 is the incremental area on the sphere at distance r from the particle and
940 normal to r. dP is then

941 $dP = I(\theta)\, dA_0 / r^2$. (A4)

942 For the PMS model, dA_0 is a small rectangle with width w and height $rd\theta$, where w is the width
943 of the strip on the photodiode, and $d\theta$ is the differential scattering angle.

944 $dA_0 = r\, d\theta \times w$, where w is the width of the strip on the photodiode. From Fig. A1, $r = b/\sin(\theta)$,
945 where b is the distance from the laser to the photodiode.

946 $d\Omega = dA_0 / r^2 = (r\, d\theta \times w)/ r^2 = d\theta \times (w/r) = (w/b) \times \sin(\theta)d\theta$. (A5)

947 The incremental power across the solid angle $d\Omega$ normal to r is then

948 $dP = I(\theta) \times dA_0/ r^2 = I(\theta) \times (w/b) \times \sin(\theta)d\theta$. (A6)

949 Substituting for $I(\theta)$,

950 $dP(g,x,\theta) = [F_0\, (\lambda/2\pi)^2\, |S_1(\theta,D_p)|^2] \times (w/b) \times \sin(\theta)\, d\theta$. (A7)

951 Equation A7 can be further simplified by combining the constants into $K = (\lambda/2\pi)^2\, F_0 w/b$, where
952 K has units of watts:

953 $dP(g,x,\theta) = K\, |S_1(\theta,D_p)|^2\, \sin(\theta)\, d\theta$. (A8)

954 The power received by the photodiode from a particle of diameter D_p in the volume element at x
955 is obtained by numerically integrating across θ on the photodiode:

956 $P(m,D_p) = K\int_{\theta1(x)}^{\theta2(x)} |S_1(m,\theta,D_p)|^2\, \sin(\theta)\, d\theta$. (A9)

957 Due to the PMS geometry, the upper and lower angular scattering integration limits for θ depend
958 on the location x. This can be seen in Fig. S4. For example, at x = 0 mm, the upper and lower
959 integration limits for θ are 18 to 38 degrees. At x = 4.0 mm, over the center of the photodiode,
960 the angular integration limits are 50 to 130 degrees.

961 The total power P in Watts received by the photodiode from the light scattered by all the
962 particles of diameter D_p in the laser is obtained by carrying out the numerical integration in Eq.
963 A9 for all x from 0 to 10 mm:

964     $P(m,D_p) = K \int_{x=0}^{x=10mm} \int_{\theta 1(x)}^{\theta 2(x)} |S_1(m,\theta,D_p)|^2 \sin(\theta)\, d\theta\, dx.$ (A10)

965 The result for carrying out this calculation for the power per particle of size D_p is in Table S6 for
966 wavelength 657 nm and particle refractive index 1.53+0.015i. The total power received at the
967 photodiode by a distribution of particles is obtained by summing up the power per particle of size
968 D_p times the number of particles $N(D_p, m)$ in the size interval D_p to $D_p + dD_p$.

969     $P = K \int_{Dp} \int_{x=0}^{x=10mm} \int_{\theta 1(x)}^{\theta 2(x)} |S_1(m,\theta,D_p)|^2 \sin(\theta)\, N(D_p, m)\, d\theta\, dx\, dD_p.$ (A11)

970 Figure A1 shows the PMS geometry. The distance along the laser is the variable x, which ranges
971 from 0 to 10 mm. The distance along the photodiode is the variable g, which ranges from 0 to 3.0
972 mm. The distance between the photodiode and the laser is b, approximately 1.8 mm.

Code and data availability

974 Data sets are available on Zenodo.org. The dataset is available at
975 https://doi.org/10.5281/zenodo.5764982. The data were published on 15 December 2021.
976 Citation is: Ouimette, James; Malm, William; Schichtel, Bret; Sheridan Patrick; Andrews,
977 Elisabeth; Ogren, John A.; & Arnott, W. Patrick. (2021). Datasets for paper "Evaluating the
978 PurpleAir monitor as an aerosol light scattering instrument" (1.0_20211215) [Data set]. Zenodo.
979 https://doi.org/10.5281/zenodo.5764982

Supplement

981 I think ACP fills out this. We have provided the supplement to them.
982

Author contributions

984 PJS and JRO designed the field study. PJS provided measurement data from the MLO and BOS
985 sites. BAS performed the uncertainty and precision analyses. WCM led the physical-optical
986 model development with BAS and JRO. JRO and WCM performed analysis of laboratory and
987 field data for model evaluation. WPA provided insight regarding the laser behavior and
988 instrument electronics. JAO and WCM independently performed the statistical analyses of the
989 TSI nephelometer and PA data. JAO and JRO performed measurements and tests to characterize
990 the PMS5003. EA led the manuscript submission and review process. All authors read and
991 commented on the article.
992

Competing interests

994 The authors declare that they have no conflict of interest.
995

Acknowledgements

997 The authors acknowledge the following for their contributions:
998 Jim Wendell, NOAA, for engineering support, Marty Martinsen, NOAA, for MLO field support,
999 Derek Hageman, CIRES, University of Colorado, for data acquisition and processing support,
1000 and Helene Bennett, CIRA, Colorado State University, for technical editing support. The

National Park Service participation in this project was supported under the cooperative agreement P17AC00971.

Disclaimer

The assumptions, findings, conclusions, judgments, and views presented herein are those of the authors and should not be interpreted as necessarily representing NOAA or National Park Service policies. Reference to any companies or specific commercial products does not constitute endorsement by NOAA or the National Park Service.

References

Abu-Rahmah, A., Arnott, W. P., and Moosmuller, H.: Integrating nephelometer with a low truncation angle and an extended calibration scheme, Meas. Sci. Technol. 17, 1723-1732, DOI 10.1088/0957-0233/17/7/010, 2006.

Anderson, T. L. and Ogren, J. A.: Determining aerosol radiative properties using the TSI 3563 integrating nephelometer, Aerosol Sci. Technol., 29, 57-69, DOI 10.1080/02786829808965551, 1998.

Anderson, T. L., Covert, D. S., Marshall, S. F., Laucks, M. L., Charlson, R. J., Waggoner, A. P., Ogren, J. A., Caldow, R., Holm, R. L., Quant, F. R., Sem, G. J., Wiedensohler, A., Ahlquist, N. A., and Bates, T. S.: Performance characteristics of a high-sensitivity, three-wavelength, total scatter/backscatter nephelometer, J. Atmos. Oceanic Technol., 13, 967-986, DOI 10.1175/1520-0426(1996)013<0967:Pcoahs>2.0.Co;2, 1996.

Andrews, E., Sheridan, P. J., Ogren, J. A., Hageman, D., Jefferson, A., Wendell, J., Alastuey, A., Alados-Arboledas, L., Bergin, M., Ealo, M., Hallar, A. G., Hoffer, A., Kalapov, I., Keywood, M., Kim, J., Kim, S. W., Kolonjari, F., Labuschagne, C., Lin, N. H., Macdonald, A., Mayol-Bracero, O. L., McCubbin, I. B., Pandolfi, M., Reisen, F., Sharma, S., Sherman, J. P., Sorribas, M., and Sun, J. Y.: Overview of the NOAA/ESRL Federated Aerosol Network, Bull. Am. Meteorol. Soc., 100, 123-135, DOI 10.1175/bams-d-17-0175.1, 2019.

Arnott, W. P., Walker, J. W., Moosmuller, H., Elleman, R. A., Jonsson, H. H., Buzorius, G., Conant, W. C., Flagan, R. C., and Seinfeld, J. H.: Photoacoustic insight for aerosol light absorption aloft from meteorological aircraft and comparison with particle soot absorption photometer measurements: DOE Southern Great Plains climate research facility and the coastal stratocumulus imposed perturbation experiments, J. Geophys. Res.-Atmospheres, 111, DOI 10.1029/2005jd005964, 2006.

Barkjohn, K. K., Gantt, B., and Clements, A. L.: Development and application of a United States wide correction for $PM_{2.5}$ data collected with the PurpleAir Sensor, Atmos. Meas. Tech. Discuss., DOI https://doi.org/10.5194/amt-2020-413, 2020.

Beuttell, R. G. and Brewer, A. W.: Instruments for the measurement of the visual range, J. Sci. Instr. Phys. Ind., 26, 357-359, DOI 10.1088/0950-7671/26/11/302, 1949.

Bodhaine, B. A. and Mendonca, B. G.: Preliminary four wavelength nephelometer measurements at Mauna Loa Observatory, Geophys. Res. Lett., 1, 119-122, DOI 10.1029/GL001i003p00119, 1974.

Bodhaine, B. A., Mendonca, B. G., Harris, J. M., and Miller, J. M.: Seasonal variations in aerosols and atmospheric transmission at Mauna Loa Observatory, J. Geophys. Res.-Oceans, 86, 7395-7398, DOI 10.1029/JC086iC08p07395, 1981.

Bohren, C. F. and Huffman, D. R.: Absorption and Scattering of Light by Small Particles, John Wiley & Sons, Inc., New York, ISBN 0 471 057772 X, 1983.

Brockman, J. E., Aerosol transport in lines and inlets - Sample extraction section 6.2 in *Aerosol Measurement: Principles, Techniques and Applications, 3rd Edition,* Kulkarni, P., Baron, P., and Willeke, K., eds., ISBN: 978-0-1033 470-38741-2, 2011.

Butcher, S. S. and Charlson, R. J.: An Introduction to Air Chemistry, Academic Press, https://doi.org/10.1016/B978-0-12-148250-3.X5001-X, ISBN 978-0-12-148250-3, 1972.

Chambers, S. D., Zahorowski, W., Williams, A. G., Crawford, J., and Griffiths, A. D.: Identifying tropospheric baseline air masses at Mauna Loa Observatory between 2004 and 2010 using Radon-222 and back trajectories, J. Geophys. Res.-Atmospheres, 118, 992-1004, DOI 10.1029/2012jd018212, 2013.

Currie, L. A.: Limits for qualitative detection and quantitative determination - Application to radiochemistry, Anal. Chem., 40, 586-&, DOI 10.1021/ac60259a007, 1968.

Friedlander, S. K.: Smoke, Dust and Haze: Fundamentals of Aerosol Behavior, Wiley, New York, 333 pp., ISBN 10: 0471014680,13: 9780471014683, 1977.

Gliss, J., Mortier, A., Schulz, M., Andrews, E., Balkanski, Y., Bauer, S. E., Benedictow, A. M. K., Bian, H., Checa-Garcia, R., Chin, M., Ginoux, P., Griesfeller, J. J., Heckel, A., Kipling, Z., Kirkevag, A., Kokkola, H., Laj, P., Le Sager, P., Lund, M. T., Myhre, C. L., Matsui, H., Myhre, G., Neubauer, D., van Noije, T., North, P., Olivi, D. J. L., Remy, S., Sogacheva, L., Takemura, T., Tsigaridis, K., and Tsyro, S. G.: AeroCom phase III multi-model evaluation of the aerosol life cycle and optical properties using ground- and space-based remote sensing as well as surface in situ observations, Atmos. Chem. Phys., 21, 87-128, DOI 10.5194/acp-21-87-2021, 2021.

Grinshpun, S., Willeke, K., and Kalatoor, S.: A general equation for aerosol aspiration by thin-walled sampling probes in calm and moving air, Atmos. Environ. Part a-General Topics, 27, 1459-1470, DOI 10.1016/0960-1686(93)90132-i, 1993.

Gupta, P., Doraiswamy, P., Levy, R., Pikelnaya, O., Maibach, J., Feenstra, B., Polidori, A., Kiros, F., and Mills, K. C.: Impact of California fires on local and regional air quality: The role of a low-cost sensor network and satellite observations, Geohealth, 2, 172-181, DOI 10.1029/2018gh000136, 2018.

Hagan, D. H. and Kroll, J. H.: Assessing the accuracy of low-cost optical particle sensors using a physics-based approach, Atmos. Meas. Tech., 13, 6343-6355, DOI 10.5194/amt-13-6343-2020, 2020.

Hand, J. L., and Malm, W. C.: Review of aerosol mass scattering efficiencies from ground-based measurements since 1990, J. Geophys. Res., 112, D16203, doi:10.1029/2007JD008484, 2007.

Hangal, S. and Willeke, K.: Aspiration efficiency - Unified model for all forward sampling angles, Environ. Sci. Technol., 24, 688-691, DOI 10.1021/es00075a012, 1990.

Harris, J. M. and Kahl, J. D.: A descriptive atmospheric transport climatology for the Mauna Loa Observatory, using clustered trajectories, J. Geophys. Res.-Atmospheres, 95, 13651-13667, DOI 10.1029/JD095iD09p13651, 1990.

He, M. L., Kuerbanjiang, N., and Dhaniyala, S.: Performance characteristics of the low-cost plantower PMS optical sensor, Aerosol Sci. Technol., 54, 232-241, DOI 10.1080/02786826.2019.1696015, 2020.

Heintzenberg, J. and Charlson, R. J.: Design and applications of the integrating nephelometer: A review, J. Atmos. Oceanic Technol., 13, 987-1000, DOI 10.1175/1520-0426(1996)013<0987:Daaoti>2.0.Co;2, 1996.

Heintzenberg, J., Wiedensohler, A., Tuch, T. M., Covert, D. S., Sheridan, P., Ogren, J. A., Gras, J., Nessler, R., Kleefeld, C., Kalivitis, N., Aaltonen, V., Wilhelm, R. T., and Havlicek, M.: Intercomparisons and aerosol calibrations of 12 commercial integrating nephelometers of three manufacturers, J. Atmos. Oceanic Technol., 23, 902-914, DOI 10.1175/jtech1892.1, 2006.

Hering, S. V.: Impactors, cyclones, and other inertial and gravitational collectors, in *Air Sampling Instruments for Evaluation of Atmospheric Contaminants,* Cohen, B.S., Hering, S.V. (eds.), proceedings of the American Conference of Governmental Industrial Hygienists, Cincinnati, 279-289, ISBN 1882417089 9781882417087, http://calliope.dem.uniud.it/CLASS/DES-IND-PLA1/impactorscyclonesch14p1.pdf, 1995.

Holder, A. L., Mebust, A. K., Maghran, L. A., McGown, M. R., Stewart, K. E., Vallano, D. M., Elleman, R. A., and Baker, K. R.: Field evaluation of low-cost particulate matter sensors for measuring wildfire smoke, Sensors, 20, 17, DOI 10.3390/s20174796, 2020.

Hyslop, N. P. and White, W. H.: An empirical approach to estimating detection limits using collocated data, Environ. Sci. Technol., 42, 5235-5240, DOI 10.1021/es7025196, 2008.

Hyslop, N. P. and White, W. H.: Estimatingprecision using duplicate measurements, J. Air Waste Manage. Assoc., 59, 1032-1039, DOI 10.3155/1047-3289.59.9.1032, 2009.

Jayaratne, R., Liu, X. T., Ahn, K. H., Asumadu-Sakyi, A., Fisher, G., Gao, J., Mabon, A., Mazaheri, M., Mullins, B., Nyaku, M., Ristovski, Z., Scorgie, Y., Thai, P., Dunbabin, M., and Morawska, L.: Low-cost PM2.5 sensors: An assessment of their suitability for various applications, Aerosol Air Qual. Res., 20, 520-532, DOI 10.4209/aaqr.2018.10.0390, 2020.

JCGM100:GUM: Evaluation of measurement data — Guide to the Expression of Uncertainty in Measurement, International Standardization Organization, Geneva, accessed 22 March 2021, https://www.bipm.org/en/publications/guides/gum.html, 2008.

Kelly, K. E., Whitaker, J., Petty, A., Widmer, C., Dybwad, A., Sleeth, D., Martin, R., and Butterfield, A.: Ambient and laboratory evaluation of a low-cost particulate matter sensor, Environ. Pollut., 221, 491-500, DOI 10.1016/j.envpol.2016.12.039, 2017.

Kuula, J., Makela, T., Aurela, M., Teinila, K., Varjonen, S., Gonzalez, O., and Timonen, H.: Laboratory evaluation of particle-size selectivity of optical low-cost particulate matter sensors, Atmos. Meas. Tech., 13, 2413-2423, DOI 10.5194/amt-13-2413-2020, 2020.

Laj, P., Bigi, A., Rose, C., Andrews, E., Myhre, C. L., Collaud Coen, M., Lin, Y., Wiedensohler, A., Schulz, M., Ogren, J. A., Fiebig, M., Gliss, J., Mortier, A., Pandolfi, M., Petaja, T., Kim, S. W., Aas, W., Putaud, J. P., Mayol-Bracero, O., Keywood, M., Labrador, L., Aalto, P., Ahlberg,

E., Arboledas, L. A., Alastuey, A., Andrade, M., Artinano, B., Ausmeel, S., Arsov, T., Asmi, E., Backman, J., Baltensperger, U., Bastian, S., Bath, O., Beukes, J. P., Brem, B. T., Bukowiecki, N., Conil, S., Couret, C., Day, D., Dayantolis, W., Degorska, A., Eleftheriadis, K., Fetfatzis, P., Favez, O., Flentje, H., Gini, M. I., Gregoric, A., Gysel-Beer, M., Hallar, A. G., Hand, J., Hoffer, A., Hueglin, C., Hooda, R. K., Hyvarinen, A., Kalapov, I., Kalivitis, N., Kasper-Giebl, A., Kim, J. E., Kouvarakis, G., Kranjc, I., Krejci, R., Kulmala, M., Labuschagne, C., Lee, H. J., Lihavainen, H., Lin, N. H., Loschau, G., Luoma, K., Marinoni, A., Dos Santos, S. M., Meinhardt, F., Merkel, M., Metzger, J. M., Mihalopoulos, N., Nguyen, N. A., Ondracek, J., Perez, N., Perrone, M. R., Petit, J. E., Picard, D., Pichon, J. M., Pont, V., Prats, N., Prenni, A., Reisen, F., Romano, S., Sellegri, K., Sharma, S., Schauer, G., Sheridan, P., Sherman, J. P., Schutze, M., Schwerin, A., Sohmer, R., Sorribas, M., Steinbacher, M., Sun, J. Y., Titos, G., Toczko, B., Tuch, T., Tulet, P., Tunved, P., Vakkari, V., Velarde, F., Velasquez, P., Villani, P., Vratolis, S., Wang, S. H., Weinhold, K., Weller, R., Yela, M., Yus-Diez, J., Zdimal, V., Zieger, P., and Zikova, N.: A global analysis of climate-relevant aerosol properties retrieved from the network of Global Atmosphere Watch (GAW) Near-Surface Observatories, Atmos. Meas. Tech., 13, 4353-4392, DOI 10.5194/amt-13-4353-2020, 2020.

Malings, C., Tanzer, R., Hauryliuk, A., Saha, P. K., Robinson, A. L., Presto, A. A., and Subramanian, R.: Fine particle mass monitoring with low-cost sensors: Corrections and long-term performance evaluation, Aerosol Sci. Technol., 54, 160-174, DOI 10.1080/02786826.2019.1623863, 2020.

Malm, W. C., Sisler, J. F., Huffman, D., Eldred, R. A., and Cahill, T. A.: Spatial and seasonal trends in particle concentration and optical extinction in the United States, J. Geophys. Res., 99, 1347-1370, DOI 10.1029/93JD02916, 1994.

Markowicz, K. M. and Chilinski, M. T.: Evaluation of two low-cost optical particle counters for the measurement of ambient aerosol scattering coefficient and angstrom ngstrom exponent, Sensors, 20, DOI 10.3390/s20092617, 2020.

Mehadi, A., Moosmueller, H., Campbell, D. E., Ham, W., Schweizer, D., Tarnay, L., and Hunter, J.: Laboratory and field evaluation of real-time and near real-time $PM_{2.5}$ smoke monitors, J. Air Waste Manage. Assoc., 70, 158-179, DOI 10.1080/10962247.2019.1654036, 2020.

Middleton, W. E. K.: Vision Through the Atmosphere, University of Toronto Press, Toronto, 250 pp., ISBN 1487587104, 9781487587109, 1952.

Miller, J. M.: A 5-year climatology of back trajectories from the Mauna Loa Observatory, Hawaii, Atmos. Environ., 15, 1553-1558, DOI 10.1016/0004-6981(81)90138-4, 1981.

Molenar, J. V.: Analysis of the real world performance of the Optec NGN-2 ambient nephelometer, presented at the Air & Waste Management Association conference on Visual Air Quality: Aerosols and Global Radiation Balance, Bartlett, New Hampshire, 9-12 September, 243-265, https://www.optecinc.com/visibility/pdf/ngn_2_analysis_real_world.pdf, 1997.

Morawska, L., Thai, P. K., Liu, X. T., Asumadu-Sakyi, A., Ayoko, G., Bartonova, A., Bedini, A., Chai, F. H., Christensen, B., Dunbabin, M., Gao, J., Hagler, G. S. W., Jayaratne, R., Kumar, P., Lau, A. K. H., Louie, P. K. K., Mazaheri, M., Ning, Z., Motta, N., Mullins, B., Rahman, M. M., Ristovski, Z., Shafiei, M., Tjondronegoro, D., Westerdahl, D., and Williams, R.: Applications of low-cost sensing technologies for air quality monitoring and exposure

assessment: How far have they gone?, Environ. Int., 116, 286-299, DOI 10.1016/j.envint.2018.04.018, 2018.

Mulholland, G. W. and Bryner, N. P.: Radiometric model of the transmission cell-reciprocal nephelomeeter, Atmos. Environ., 28, 873-887, DOI 10.1016/1352-2310(94)90246-1, 1994.

Muller, T., Laborde, M., Kassell, G., and Wiedensohler, A.: Design and performance of a three-wavelength LED-based total scatter and backscatter integrating nephelometer, Atmos. Meas. Tech., 4, 1291-1303, DOI 10.5194/amt-4-1291-2011, 2011.

Nakayama, T., Suzuki, H., Kagamitani, S., Ikeda, Y., Uchiyama, A., and Matsumi, Y.: Characterization of a three wavelength Photoacoustic Soot Spectrometer (PASS-3) and a Photoacoustic Extinctiometer (PAX), J. Meteorol. Soc. Jpn., 93, 285-308, DOI 10.2151/jmsj.2015-016, 2015.

Naqwi, A. and Durst, F.: Focusing of diode laser beams - A simple mathematical model, Appl. Optics, 29, 1780-1785, DOI 10.1364/ao.29.001780, 1990.

Pandolfi, M., Alados-Arboledas, L., Alastuey, A., Andrade, M., Angelov, C., Artinano, B., Backman, J., Baltensperger, U., Bonasoni, P., Bukowiecki, N., Coen, M. C., Conil, S., Coz, E., Crenn, V., Dudoitis, V., Ealo, M., Eleftheriadis, K., Favez, O., Fetfatzis, P., Fiebig, M., Flentje, H., Ginot, P., Gysel, M., Henzing, B., Hoffer, A., Smejkalova, A. H., Kalapov, I., Kalivitis, N., Kouvarakis, G., Kristensson, A., Kulmala, M., Lihavainen, H., Lunder, C., Luoma, K., Lyamani, H., Marinoni, A., Mihalopoulos, N., Moerman, M., Nicolas, J., O'Dowd, C., Petaja, T., Petit, J. E., Pichon, J. M., Prokopciuk, N., Putaud, J. P., Rodriguez, S., Sciare, J., Sellegri, K., Swietlicki, E., Titos, G., Tuch, T., Tunved, P., Ulevicius, V., Vaishya, A., Vana, M., Virkkula, A., Vratolis, S., Weingartner, E., Wiedensohler, A., and Laj, P.: A European aerosol phenomenology-6: Scattering properties of atmospheric aerosol particles from 28 ACTRIS sites, Atmos. Chem. Phys., 18, 7877-7911, DOI 10.5194/acp-18-7877-2018, 2018.

Papapostolou, V., Zhang, H., Feenstra, B. J., and Polidori, A.: Development of an environmental chamber for evaluating the performance of low-cost air quality sensors under controlled conditions, Atmos. Environ., 171, 82-90, DOI 10.1016/j.atmosenv.2017.10.003, 2017.

Pawar, H. and Sinha, B.: Humidity, density, and inlet aspiration efficiency correction improve accuracy of a low-cost sensor during field calibration at a suburban site in the North-Western Indo-Gangetic plain (NW-IGP), Aerosol Sci. Technol., 54, 685-703, DOI 10.1080/02786826.2020.1719971, 2020.

Ryan, S.: The wind field around Mauna Loa derived from surface and balloon observations, J. Geophys. Res.-Atmospheres, 102, 10711-10725, DOI 10.1029/97jd00646, 1997.

Sayahi, T., Butterfield, A., and Kelly, K. E.: Long-term field evaluation of the Plantower PMS low-cost particulate matter sensors, Environ. Pollut., 245, 932-940, DOI 10.1016/j.envpol.2018.11.065, 2019.

Shaw, G. E.: Transport of Asian desert aerosol to the Hawaiian Islands, J. Appl. Meteorol., 19, 1254-1259, DOI 10.1175/1520-0450(1980)019<1254:Toadat>2.0.Co;2, 1980.

Sherman, J. P., Sheridan, P. J., Ogren, J. A., Andrews, E., Hageman, D., Schmeisser, L., Jefferson, A., and Sharma, S.: A multi-year study of lower tropospheric aerosol variability and systematic relationships from four North American regions, Atmos. Chem. Phys., 15, 12487-12517, DOI 10.5194/acp-15-12487-2015, 2015.

1204 Snider, G., Weagle, C. L., Martin, R. V., van Donkelaar, A., Conrad, K., Cunningham, D.,
1205 Gordon, C., Zwicker, M., Akoshile, C., Artaxo, P., Anh, N. X., Brook, J., Dong, J., Garland, R.
1206 M., Greenwald, R., Griffith, D., He, K., Holben, B. N., Kahn, R., Koren, I., Lagrosas, N., Lestari,
1207 P., Ma, Z., Martins, J. V., Quel, E. J., Rudich, Y., Salam, A., Tripathi, S. N., Yu, C., Zhang, Q.,
1208 Zhang, Y., Brauer, M., Cohen, A., Gibson, M. D., and Liu, Y.: SPARTAN: a global network to
1209 evaluate and enhance satellite-based estimates of ground-level particulate matter for global
1210 health applications, Atmos. Meas. Tech., 8, 505-521, DOI 10.5194/amt-8-505-2015, 2015.

1211 Tryner, J., L'Orange, C., Mehaffy, J., Miller-Lionberg, D., Hofstetter, J. C., Wilson, A., and
1212 Volckens, J.: Laboratory evaluation of low-cost PurpleAir PM monitors and in-field correction
1213 using co-located portable filter samplers, Atmos. Environ., 220, DOI
1214 10.1016/j.atmosenv.2019.117067, 2020.

1215 Zheng, T. S., Bergin, M. H., Johnson, K. K., Tripathi, S. N., Shirodkar, S., Landis, M. S.,
1216 Sutaria, R., and Carlson, D. E.: Field evaluation of low-cost particulate matter sensors in high-
1217 and low-concentration environments, Atmos. Meas. Tech., 11, 4823-4846, DOI 10.5194/amt-11-
1218 4823-2018, 2018.

1219 Zhou, Y.: Product data manual of PLANTOWER - PMS5003 series,
1220 https://www.aqmd.gov/docs/default-source/aq-spec/resources-page/plantower-pms5003-
1221 manual_v2-3.pdf, accessed 15 March 2021, 2016.

1222

1223

 Tables

1225 **Table 1.** Summary of PA, TSI nephelometer, and DMPS data coverage.

	number of hours				percent coverage			
site	PA-PMS	TSI neph	DMPS	overlap	PA-PMS	TSI neph	DMPS	Time period
MLO	9371	9204	na	9204	97.6	95.9	na	2019-05-06 to 2020-06-05
BOS	7716	7479	7045	6901	97.7	94.7	89.2	2020-02-13 to 2021-01-06

1226
1227
1228 **Table 2.** Summary of PA-PMS and nephelometer hourly observations at MLO and BOS.

	1 h median (average)				1 h range min-max			
	PA-PMS		TSI nephelometer		PA-PMS		TSI nephelometer	
Site	$PM_{2.5}$ $\mu g\ m^{-3}$	CH1	b_{sp10} Mm^{-1}	b_{sp1} Mm^{-1}	$PM_{2.5}$ $\mu g\ m^{-3}$	CH1	b_{sp10} Mm^{-1}	b_{sp1} Mm^{-1}
MLO	0.000 (0.12)	26.7 (75.2)	1.19 (2.82)	0.76 (1.50)	0.0 - 21.6	0.26 - 1649	-0.35 - 35.2	-0.29 - 34.2
BOS	3.37 (8.42)	720 (1422)	14.6 (32.4)	9.9 (20.9)	0.0 - 571	7.38 - 63340	-0.11 - 4097	-0.44 - 2596

1229
1230
1231 **Table 3.** Ordinary least square regression coefficients with a zero intercept and standard error for
1232 b_{sp1} and CH1 as the dependent and independent variables, respectively, for the BOS, MLO, and
1233 combined datasets. CH1 and b_{sp1} reported at STP. Also shown are the respective coefficients of
1234 determination, R^2.

Site	slope (Mm^{-1})	standard error (Mm^{-1})	1/slope (Mm)	R^2
BOS	0.015	2.68×10^{-5}	67.0	0.97
MLO	0.017	5.72×10^{-5}	59.0	0.85
Both BOS&MLO	0.015	2.07×10^{-5}	67.0	0.97

1235

1236

1237   **Figures**
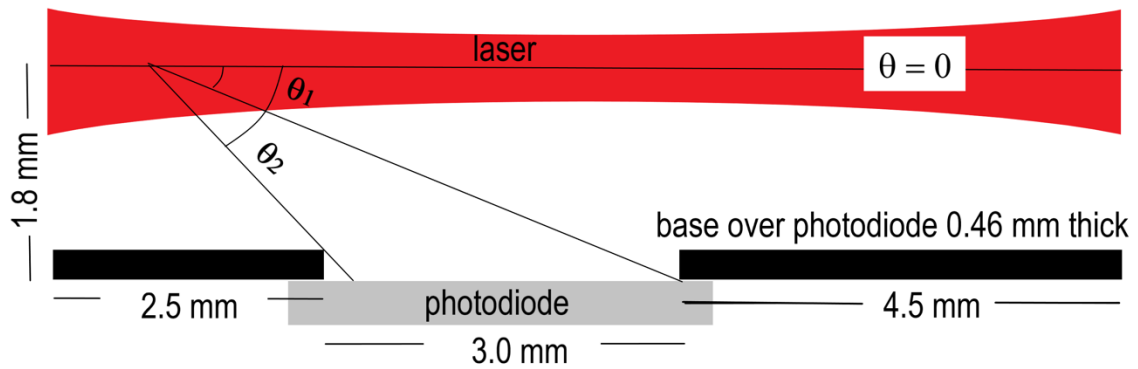
1238

1239   **Figure 1.** PMS sensor geometry highlighting the dimensions of laser beam (red) and photodiode
1240   (gray) and the various relevant distances between the two.

1241

1242
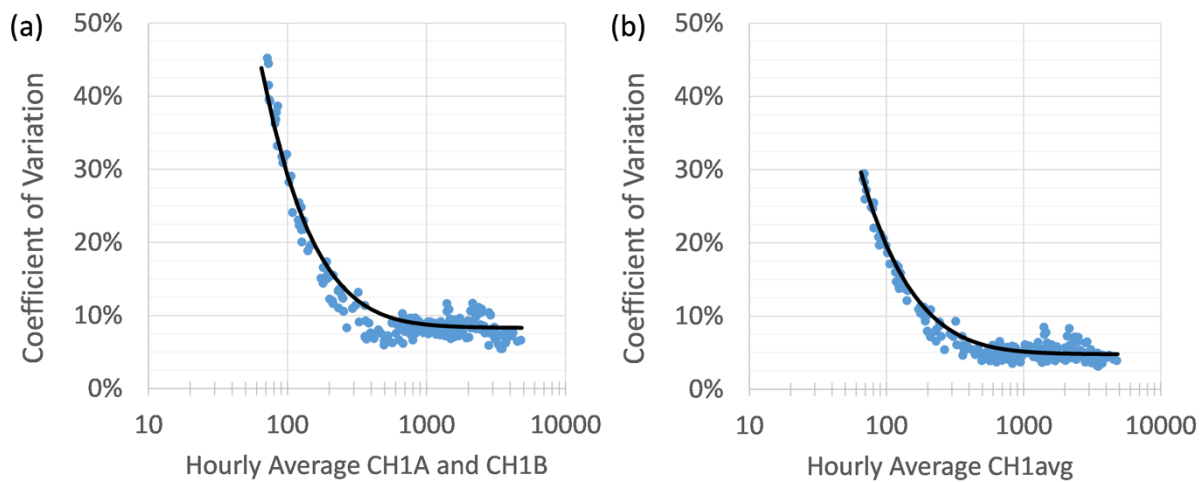
1243

1244   **Figure 2.** Precision estimated as the coefficient of variation of the hourly CH1A and CH1B (a)
1245   and CH1avg values (b) for the 19 collocated sensors and 9 PAs.

1246
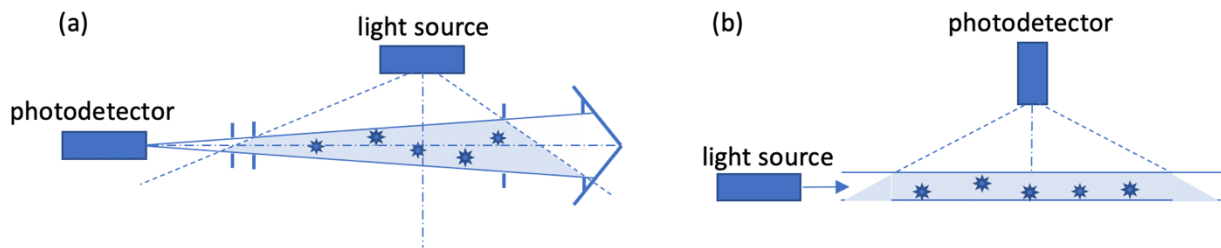
1247

Figure 3. Diagrams of the (a) cell-direct nephelometer and (b) cell-reciprocal nephelometer.

1249
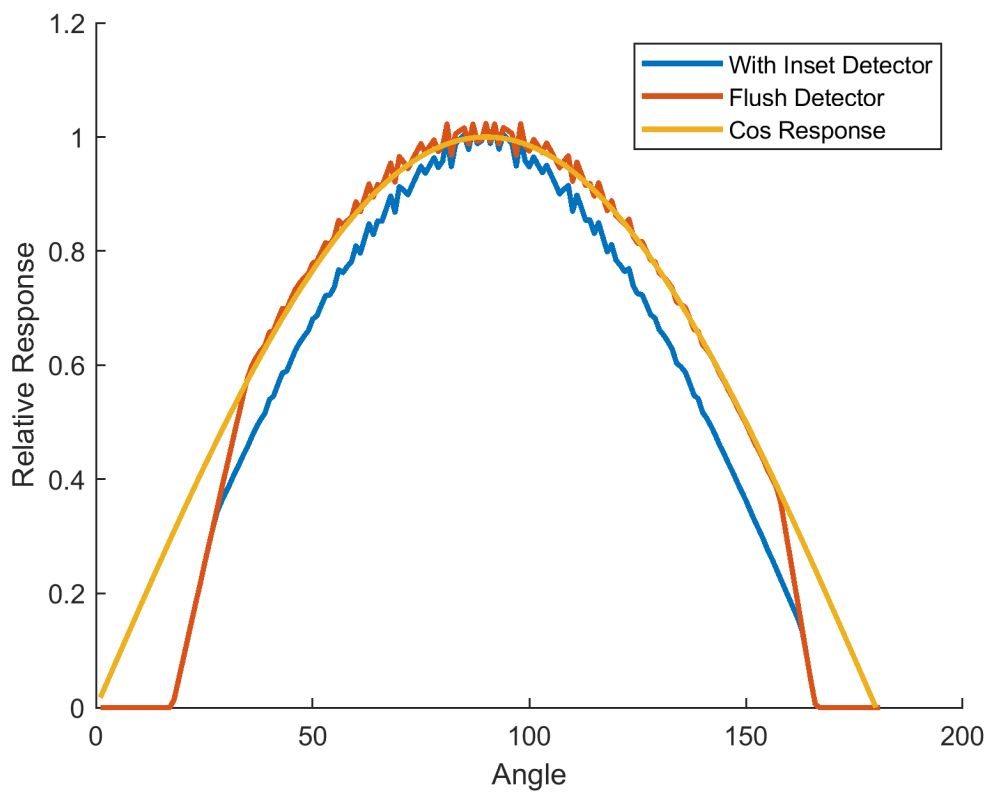
1250

Figure 4. Relative response of the photodetector resulting from truncated scattering angles and a recessed photodetector. See explanation of the different curves in text.

1253
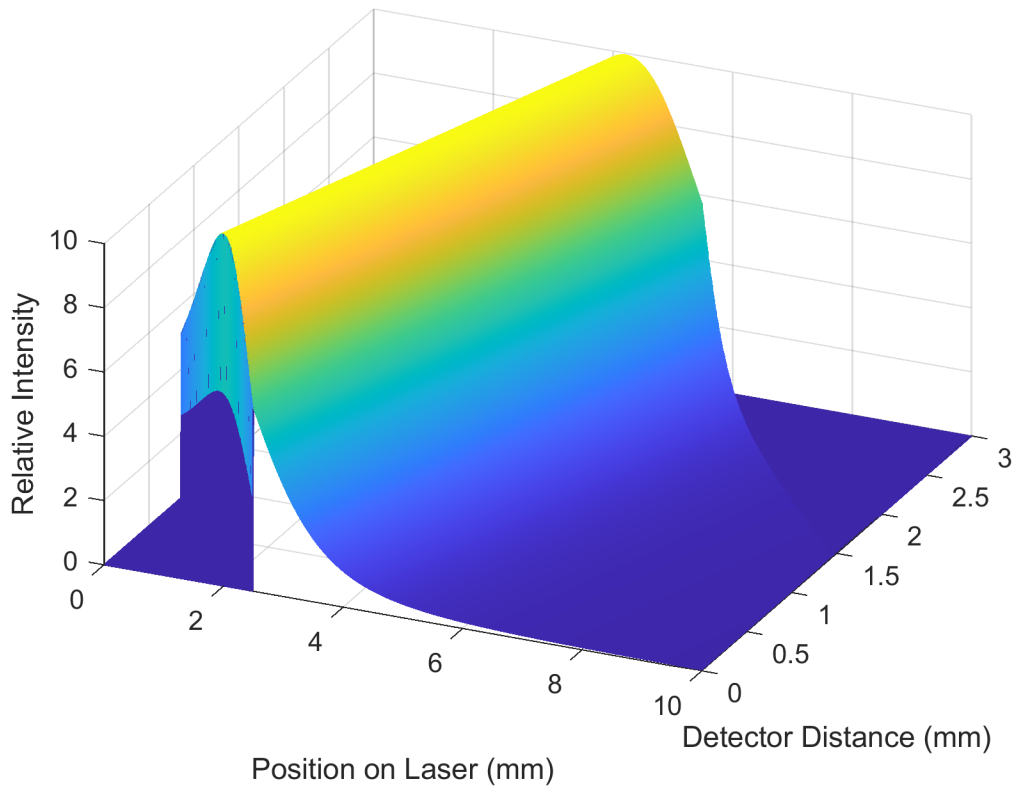
1254

1255 **Figure 5.** Relative intensity of radiant energy scattered by a lognormally distributed aerosol
1256 volume size distribution with a volume mean diameter of 0.33 µm and geometric standard
1257 deviation of 1.7 as a function of location of scattering event in the laser and as a function of
1258 position on the photodiode. Assumed laser wavelength was 650 nm, and the particle index of
1259 refraction was assumed to be 1.53. Positions in the laser and detector are from left to right as in
1260 Fig. 1 and are in units of mm.

1261
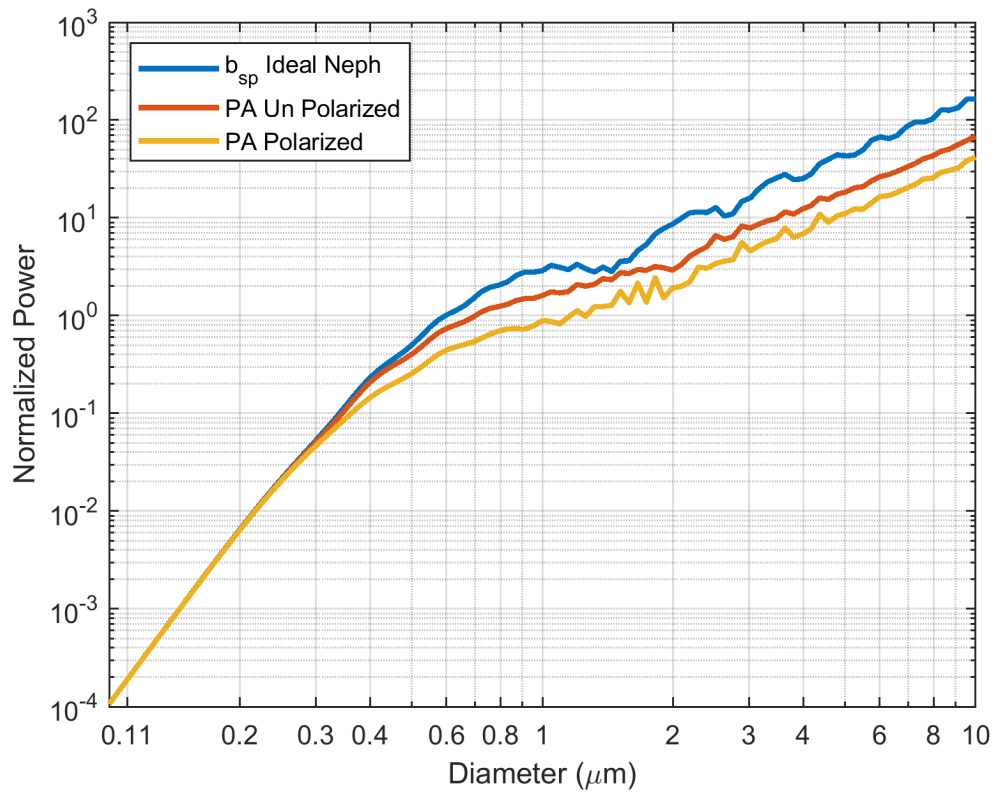
1262

Figure 6. Normalized power detected by an ideal integrating nephelometer, a PMS with an unpolarized light source, and a PMS with a perpendicularly polarized light source plotted as a function of particle diameter. Modeled light source wavelength is 657 nm, and the particle index of refraction is 1.53. See explanation of the different curves in text.

1267
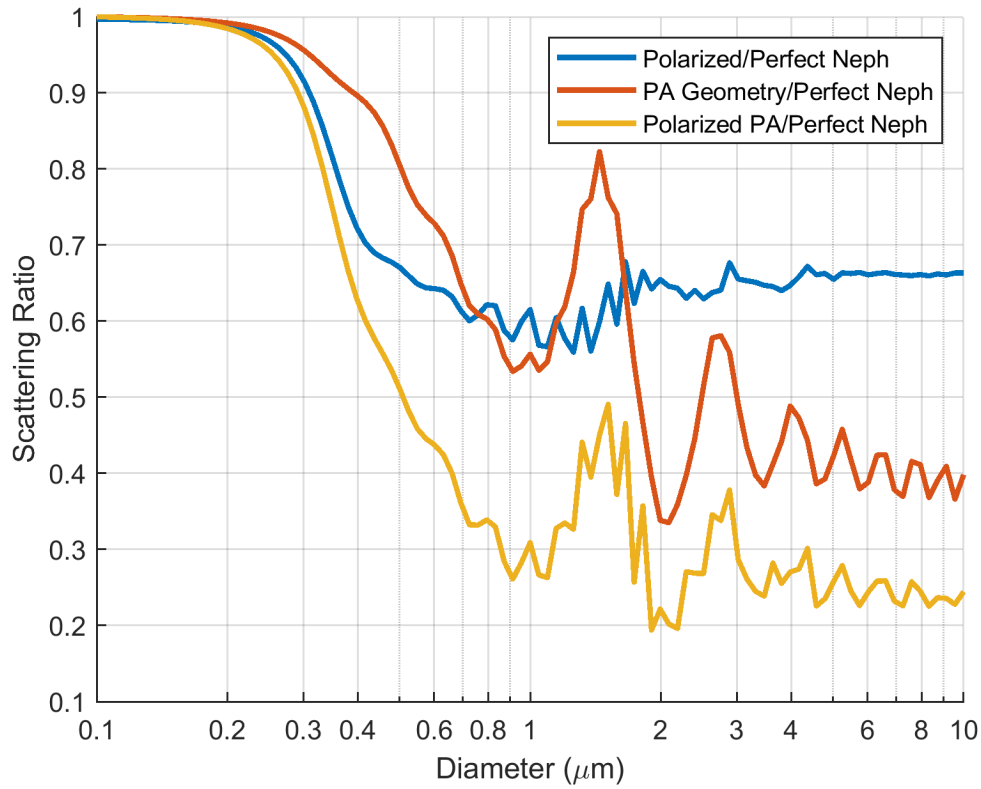
1268

Figure 7. Ratio of scattering of a "perfect" nephelometer to a nephelometer with a light source
that is perpendicularly polarized (blue) and to a PMS with an unpolarized light source (red).
Yellow line shows the effect of a perpendicularly polarized light source and PMS geometry. All
three curves are plotted as a function of particle diameter.

1273
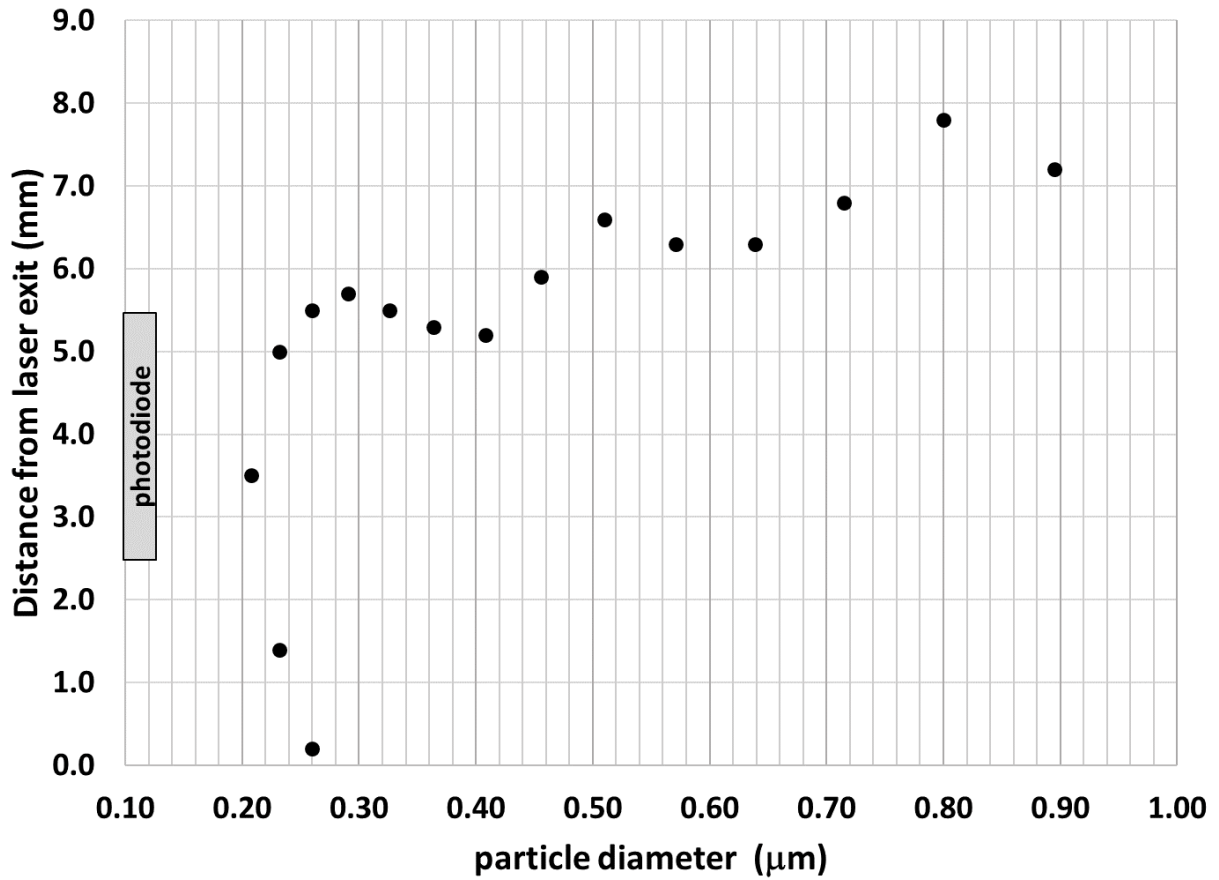
1274

1275 **Figure 8.** The model predicts that different size particles can generate the same irradiance on the
1276 photodiode, depending on their location in the laser beam. In this example, each of the particles
1277 would create 1.7×10^{-2} picowatts of scattered irradiance on the photodiode.

1278
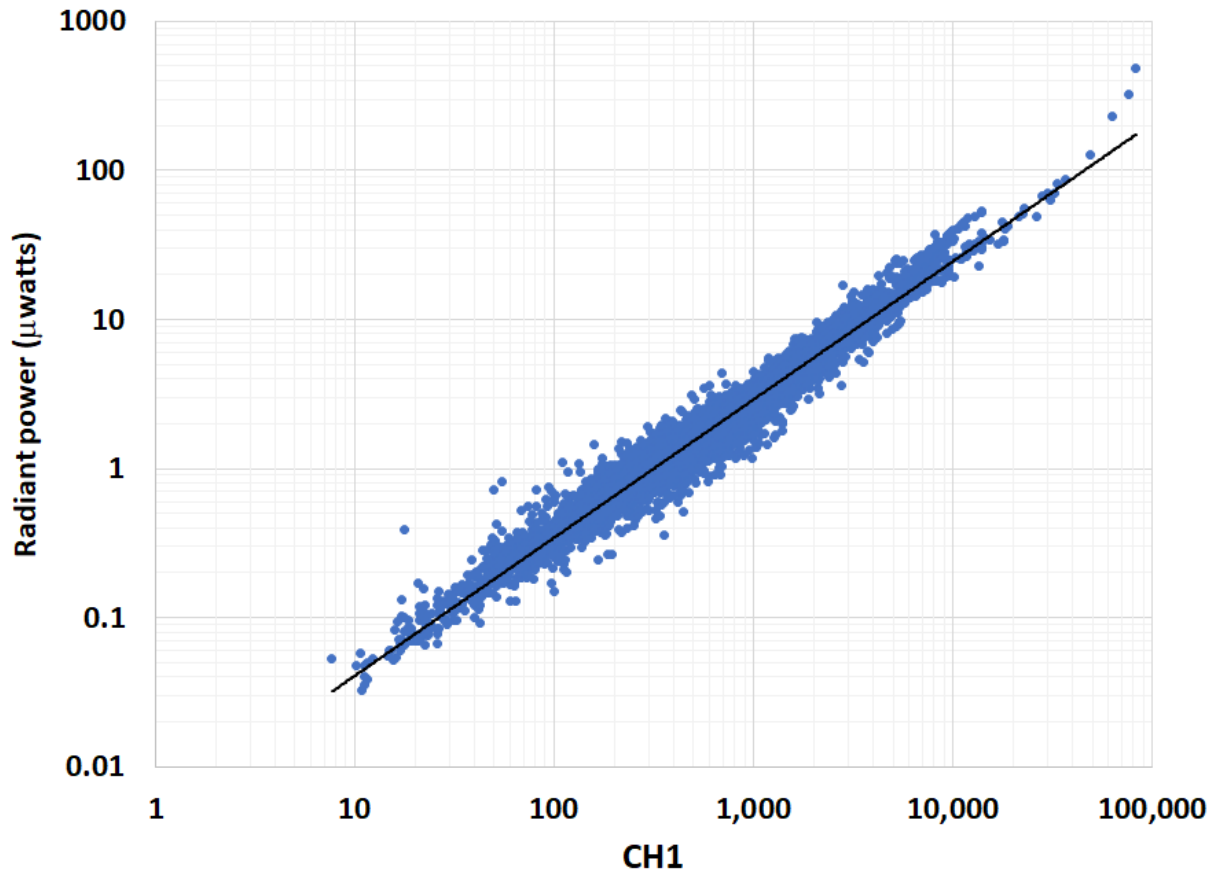
1279

1280   **Figure 9.** One hour average CH1 reported values plotted against model-predicted radiant power
1281   (or energy) in μwatts on the photodiode. Both the CH1 and DMPS data were adjusted to STP
1282   conditions. Ordinary least squares regression line is also shown. Plot is based on 6839 1 h
1283   averages at BOS.

1284
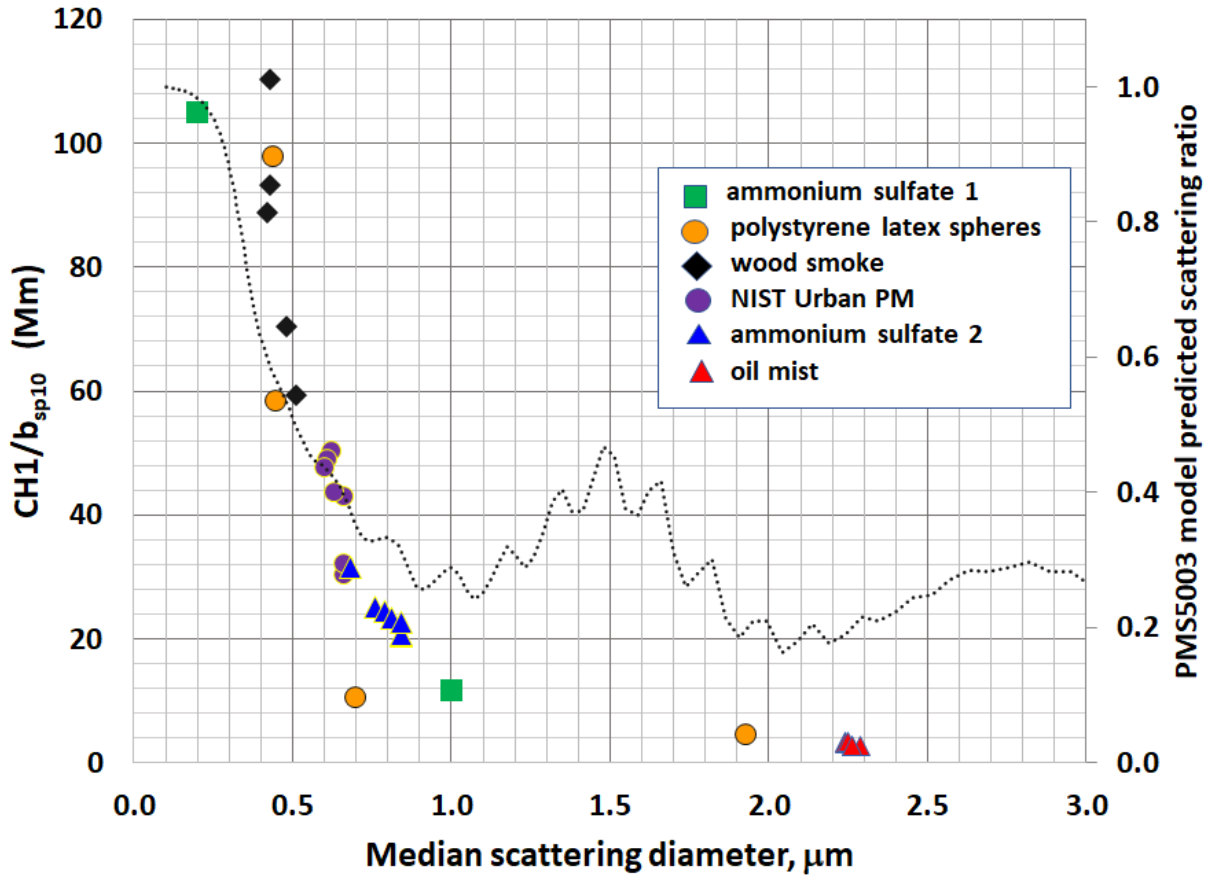
1285

Figure 10. Laboratory measurements of CH1/b_{sp10} versus median scattering diameter from Tryner et al. (2020) and He et al. (2020). Results are compared with PMS physical-optical model prediction of the scattering ratio (yellow line in Fig. 7). Maximum value of 1.0 of the model-predicted scattering ratio is arbitrarily set at a CH1/b_{sp10} value of 110 Mm. Ammonium sulfate 1 data are from He et al. (2020); all other data are from Tryner et al. (2020).

1286
1287
1288
1289
1290

1291
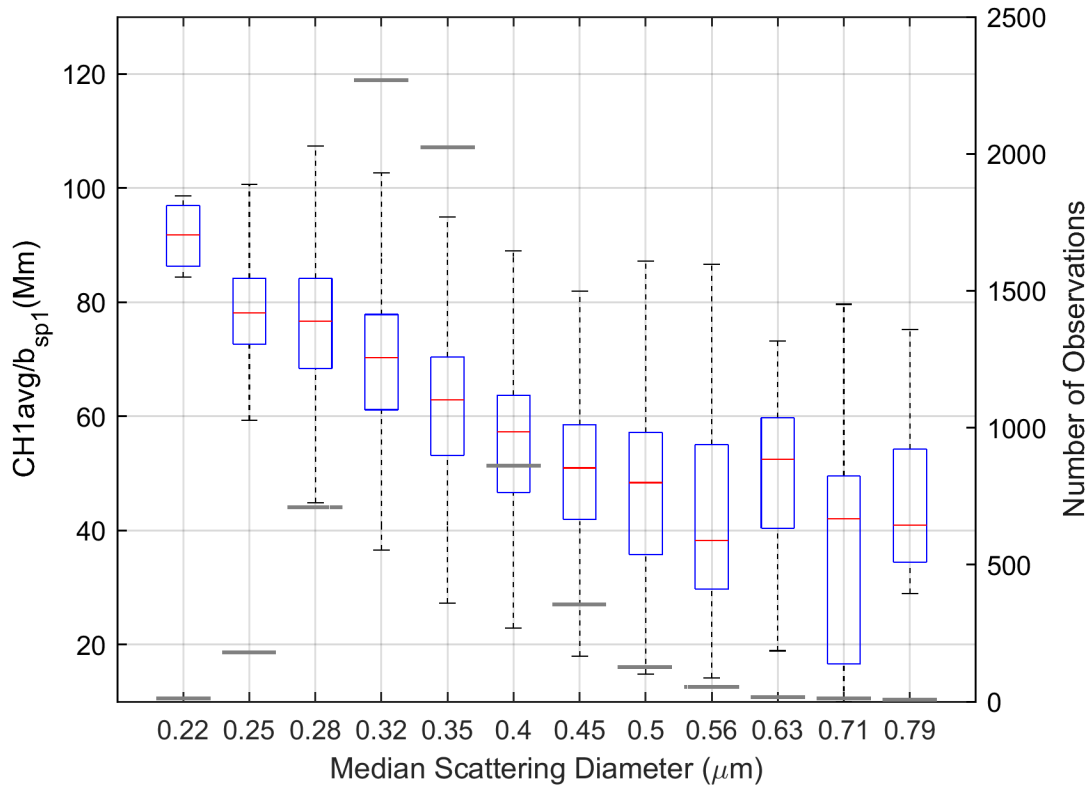
1292

Figure 11. Observed decrease in CH1avg/b_{sp1} ratio as a function of MSD values. MSD values
were selected based on a log scale but plotted equally spaced from each other to maintain
uniformity in the dimensions of the box and whisker symbol. Red line represents the median
value, and the bottom and top of each box are the first and third quartile values. Extremes shown
on each box are the 2 and 98 percentiles. Black horizontal lines for each MSD value are the
number of observations in the respective MSD bins.

1293
1294
1295
1296
1297
1298

1299
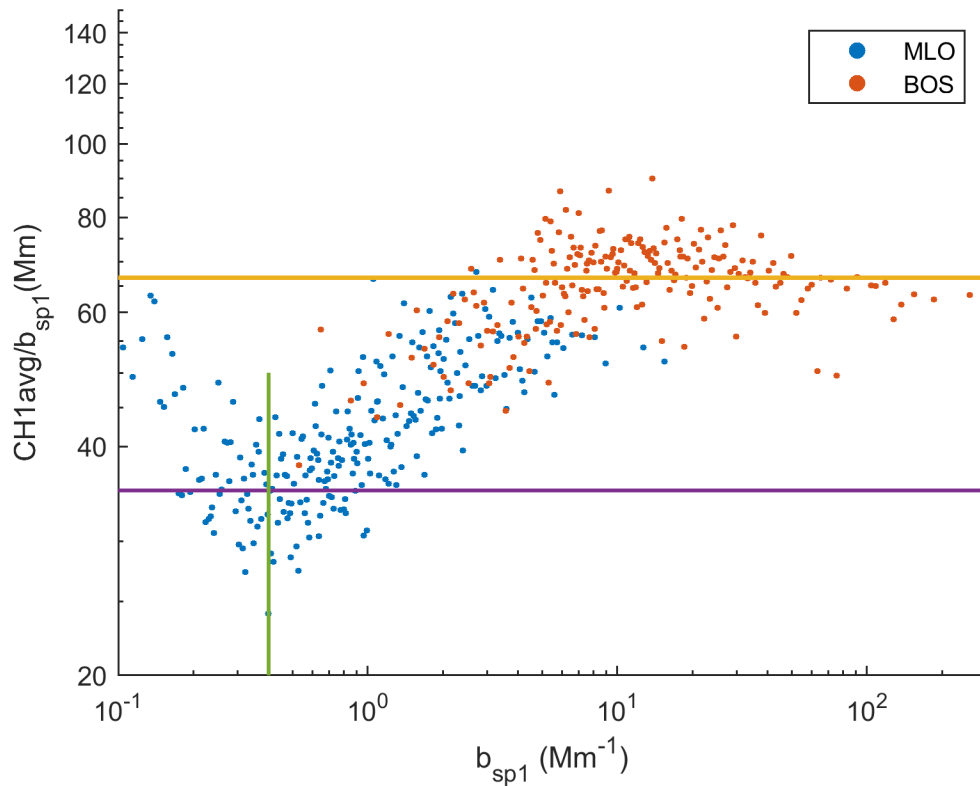
1300

Figure 12. Ratios of CH1avg and measured scattering, b_{sp1}, as a function of measured b_{sp1} for MLO and BOS. Green line corresponds to 0.4 Mm^{-1} while the purple line, a ratio of 35 Mm, corresponds to the additive uncertainty of 14. Yellow line corresponds to a CH1avg/b_{sp1} ratio of approximately 67 Mm, the slope of CH1avg vs. b_{sp1} above about 5 Mm^{-1}.

1305
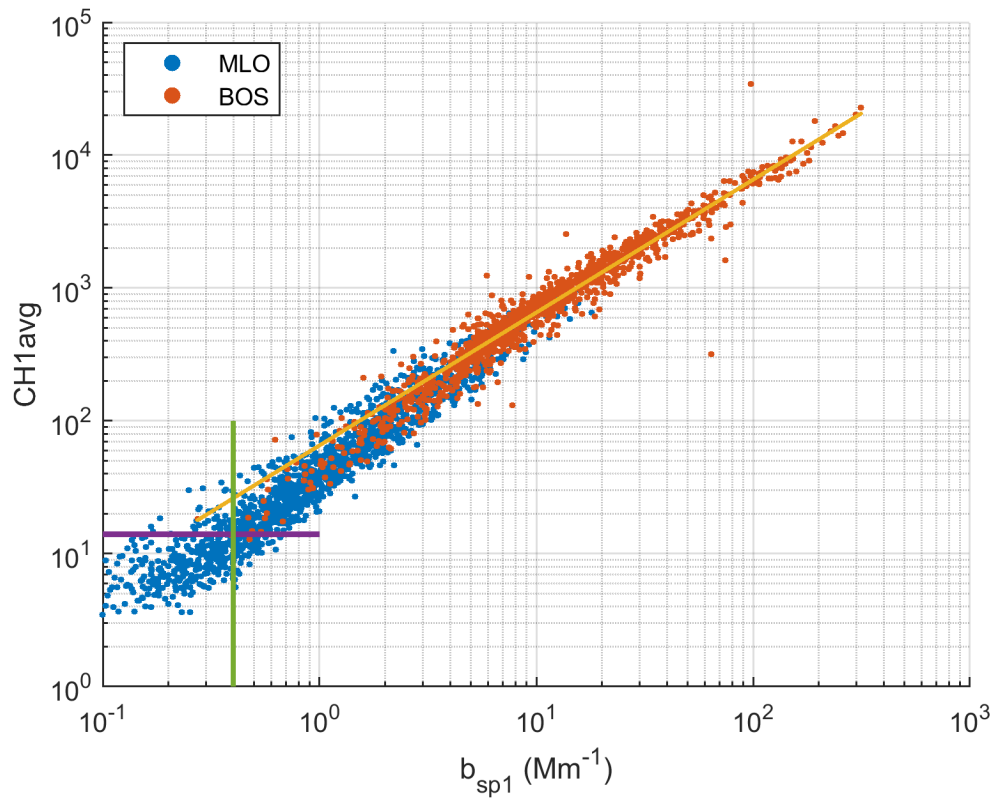
1306

1307   **Figure 13.** Fine aerosol scattering coefficient from TSI nephelometer vs. CH1avg value from
1308   PA. Yellow line represents the fit to all data. Purple line shows the additive uncertainty of 14
1309   while b_{sp1} values less than the green line were removed for the regression analysis.

1310
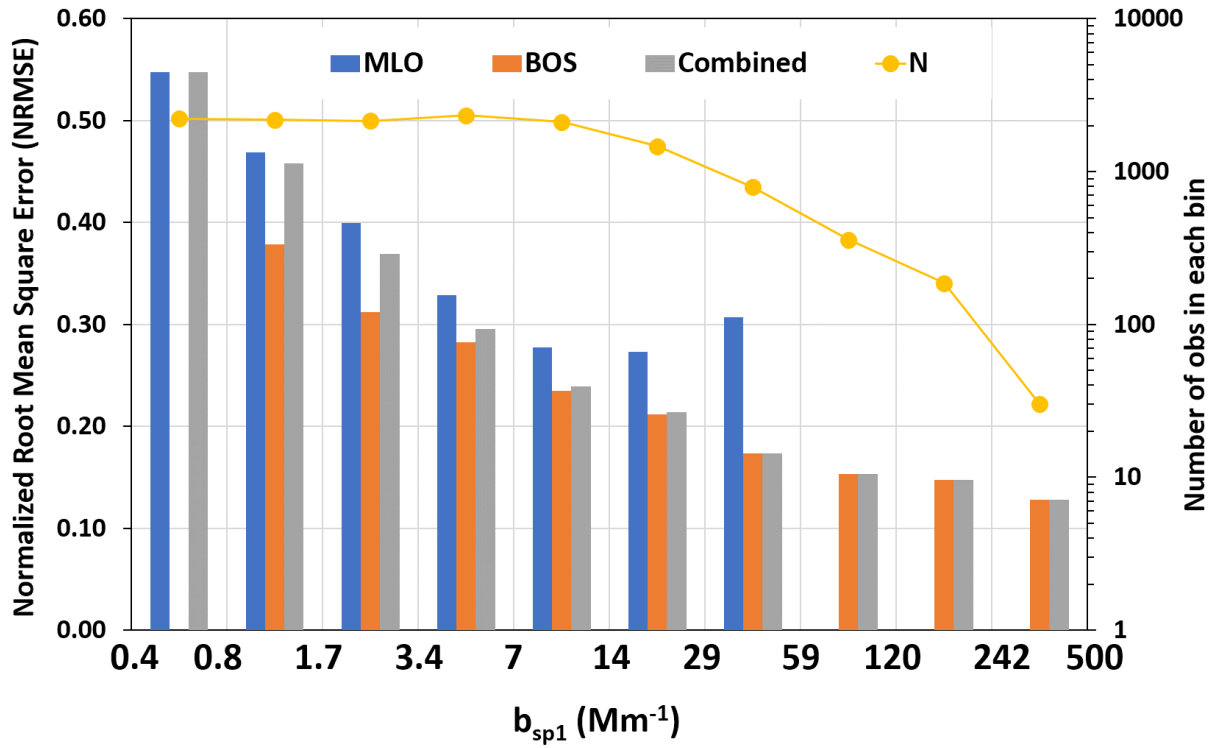
1311

1312   **Figure 14.** Normalized root mean square error between measured and estimated scattering from
1313   CH1 values plotted as a function of binned b_{sp1} for the BOS, MLO, and combined datasets.
1314   Yellow line is referenced to the right axis to provide the number of observations in each bin.
1315   Numbers on the x-axis represent the lower and upper levels of each scattering bin.

1316

differential volume element at distance x along the laser, scattering light at angle θ to the photodiode

$r = b/\sin(\theta)$

$\sin(\theta) = (r\, d\theta)/dg$

$dg = (r\, d\theta)/\sin(\theta) = (b\, d\theta)/\sin^2(\theta)$
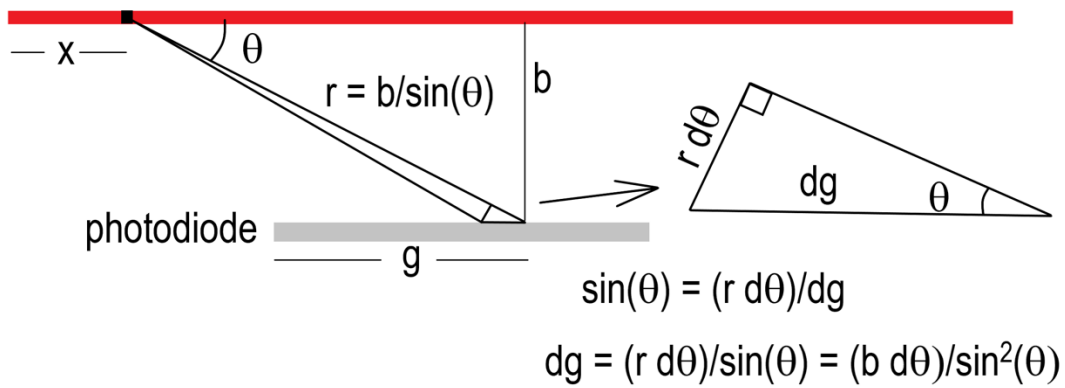
1317

1318   **Figure A1.** Sketch of PMS5003 geometry.